Åbo Akademi University

Jingxin Sui

Initial Stages of Alkali Salt Induced High Temperature Corrosion Mechanisms –

Experimental studies using a combination of chronoamperometry, scanning electron microscopy, X-ray photoelectron spectroscopy and time-of-flight secondary ion mass spectrometry

Jingxin Sui

Born 1987, Jinan, Shandong, P.R. China

B. Sc. Applied Chemistry, 2009
Qilu University of Technology, Jinan, Shandong, China

M.Sc. Chemical Engineering, 2011
Åbo Akademi University, Turku/ Åbo, Finland

Ph.D. studies at the Laboratory of Inorganic Chemistry from Feb. 2014
Åbo Akademi University, Turku/ Åbo, Finland

Initial Stages of Alkali Salt Induced High Temperature Corrosion Mechanisms –

Experimental studies using a combination of chronoamperometry, scanning electron microscopy, X-ray photoelectron spectroscopy and time-of-flight secondary ion mass spectrometry

Jingxin Sui

Laboratory of Inorganic Chemistry
Åbo Akademi

Supervisors

D.Sc. Juho Lehmusto
Åbo Akademi University

D.Sc. Mikael Bergelin
Turku PET-Centre

Professor Mikko Hupa
Åbo Akademi University

Professor Leena Hupa
Åbo Akademi University

Opponent and reviewer

Associate Professor Jesper Liske
Chalmers University of Technology

Reviewer

Assistant Professor Grzegorz Lisak
Nanyang Technological University

978-952-12-3868-0 (printed)
978-952-12-3869-7 (digital)
Painosalama Oy – Turku, Finland 2019

Preface

This thesis was carried out at the Laboratory of Inorganic Chemistry, Åbo Akademi University (ÅA), Finland within CLIFF project (2014-2017). Other research partners in the project were VTT Technical Research Centre of Finland, Lappeenranta University of Technology, Aalto University and Tampere University of Technology. Support from the National Technology Agency of Finland (Tekes), Andritz Oy, Valmet Technologies Oy, Sumitomo SHI FW, UPM-Kymmene Oyj, Clyde Bergemann GmbH, International Paper Inc., and Top Analytica Oy Ab were gratefully acknowledged.

I am deeply grateful to my supervisor, Dr. Juho Lehmusto, for his constructive criticism and relevant feedback. Without his push, I would not have finished my doctoral study! My great appreciation is also to my supervisor, Dr. Mikael Bergelin, for his great support during my stay in Finland. He supported my research and guided me patiently into the world of electrochemistry. He also gave me suggestions for purchasing cars and apartments. I am very grateful to Prof. Mikko Hupa for his trust and offering me the opportunity to work in the laboratory. His knowledge and experience always helped me both in my study and life. I wish to express my sincere thanks to my supervisor Prof. Leena Hupa. She encouraged me a lot whenever I encounter difficulties, especially, for her help at the end of my doctoral study to receive financial support and to modify the thesis and the last manuscript.

I would like to thank all my co-authors and colleagues, and the personnel at the Inorganic chemistry laboratory: their strong help and guidance made this thesis possible. I would like to thank Mr. Jyrki Juhanoja at Top Analytica for sharing his expertise in sample analysis via XPS and ToF-SIMS. I would like to express my gratitude to Dr. Patrik Yrjas and Dr. Bengt-Johan Skrifvars for acting as co-author of the publications.

I would like also to give my appreciation to Mr. Linus Silvander for his invaluable work in creating SEM images and analyses. Mr. Jan-Erik Eriksson for his help with my experiment setup and also for his advice in the everyday life. I would also like to thank Mr. Peter Uppstu for giving me some suggestion with living in Finland.

Finally, I would like to express my great appreciation to my wife Chen Tan, my mother and other family members who have always supported and accompanied me. I need to mention my cute angel Nicole. You make me a happy Daddy! Special thanks go to all my Chinese friends in Finland. You all make my life more colorful.

非常感谢现在来听我答辩的各位，也十分感谢我们轻院的兄弟姐妹们，是你们让我在芬兰感受到家的温暖。感谢那些在我最困难的时候给我送来关怀的朋友们，是你们让我重获新生。感谢所有陪我一起疯过玩过朋友们，不论你们现在身在世界的哪一个角落，我都希望你们可以一直开开心心的。特别要感谢支持我留学的母亲和不管是在学业上还是在生活上都无条件支持我的老婆。感谢那些曾出现在我生命中的每一个人，是你们让我成为了现在的我！

行路难

金樽清酒斗十千，玉盘珍羞直万钱。停杯投箸不能食，拔剑四顾心茫然。
欲渡黄河冰塞川，将登太行雪满山。闲来垂钓碧溪上，忽复乘舟梦日边。
行路难！行路难！多歧路，今安在？长风破浪会有时，直挂云帆济沧海 。

Jan. 2019
Turku
Jingxin Sui

Abstract

Various environmental problems, such as global warming, are related to the extensive use of fossil fuels. To solve these environmental problems, several renewable energy resources (RES) to substitute fossil fuels have drawn much attention. The renewable energy resource biomass has been widely used as an energy source via combustion to produce heat due to its CO_2-neutrality, availability, and various regulatory benefits. However, biomass typically contains considerable amounts of corrosive compounds, which can be released into the flue gas during the combustion process. These corrosive gaseous species may directly cause gas phase-induced corrosion, or condense and deposit on the superheater tubes in the boiler, which then causes deposit corrosion and decreases the lifespan of the superheaters. Among the corrosive compounds, alkali salts have been cited to be the most influential corrosive species, because they exist naturally and extensively in various biomasses. Alkali induced high-temperature corrosion has been extensively studied. However, little work has been done to illustrate the mechanisms of the very initial stage corrosion reactions.

In this work, a novel combinatory analysis method combining chronoamperometry (CA), X-ray photoelectron spectroscopy (XPS) and scanning electron microscopy (SEM) is proposed. In this method, CA has been utilized to detect variations in the current flow due to oxidation/reduction reactions, allowing for time-separation of different stages at the onset of the corrosion process, whereas XPS and SEM have been used for studying morphology, thickness, and composition of the formed oxide layers. In Papers I-III, this method was developed by studying the effect of three alkali salts (KCl, NaCl and K_2CO_3) on the initial corrosion mechanism of a typical superheater tube material (Sanicro 28 (Fe31Cr27Ni)). By utilizing this combinatory method, the effect of the cations (K^+ and Na^+) and anions (Cl^- and CO_3^{2-}) on the initial stage of the corrosion process has been studied. In addition to the corrosive salts, the water content in the biomass fuel is usually high, thus the effect of water vapor cannot be ignored when studying corrosion during the real biomass combustion process. To interpret the role of the water vapor in the corrosion mechanism, flowing dry and humid conditions were utilized in the experiment setup in Paper IV. Since the role of water was found to be essential in the Paper IV, the role of different sources of oxygen (water and air) in the corrosion mechanism was studied more thoroughly. Thus, in Paper V, an additional technique

in which Time-of-Flight Secondary Ion Mass Spectrometry (ToF-SIMS) and water with the stable oxygen-18 (^{18}O) isotope as a tracer of the oxygen source were utilized to track the detailed reaction mechanisms involved in the oxidation/corrosion process.

From several series of laboratory tests, it was found that at both 450 and 535 °C, all three alkali salts affected the steel and initiated alkali chromate formation within the exposure time of 2 hours. The rates of the overall corrosion reaction with all studied salts were much lower at 450 °C than at 535 °C. At the higher temperature, 535 °C, the formed chromate reacted further to chromium oxide with a significantly higher reaction rate than at 450 °C, as expected.

There were clear differences regarding the impact of cations (Na^+, K^+) and anions (Cl^-, CO_3^{2-}**)** on the initial corrosion reaction. When comparing the effect of the two cations, the two chloride salts (KCl and NaCl) had a similar influence on the overall elemental distribution in the oxide layer. Both salts led to the formation of alkali chromate, which depleted the protective oxide layer in chromium and made the stainless steel more vulnerable to high temperature corrosion. Under dry conditions, the exposure to NaCl resulted in a higher amount of sodium chromate (Na_2CrO_4) and a thicker chromium-rich layer compared to the sample exposed to KCl. Under humid conditions, the exposure to NaCl resulted in a lower amount of Na_2CrO_4 and a thicker oxide layer with a higher concentration of iron than the corresponding layers formed during the KCl exposure.

When comparing the anions (Cl^-, CO_3^{2-}), the exposure to K_2CO_3 resulted in a much higher amount of K_2CrO_4 than the exposure to KCl under dry conditions. Under humid conditions, K_2CO_3 gave rise to a much thicker and more homogeneous iron-rich oxide layer than KCl. K_2CO_3 can decompose and react with iron to form multiple intermediate products, such as iron bicarbonate ($Fe(HCO_3)_2$).

The results of this work can be utilized by material designers and boiler operators to predict material behavior under different challenging conditions in biomass combustion process.

Keywords: Stainless steel, High-temperature corrosion, Alkali salts, SEM, XPS, ToF-SIMS

Sammanfattning

Global uppvärmning och andra miljöproblem är kopplade till en utbredd användning av fossila bränslen. För att lösa vissa miljöproblem riktas nu mycket uppmärksamhet mot förnyelsebara energikällor att ersätta fossila bränslen med. Olika typer av biomassa används därför ofta som energikälla i förbränning på grund av att de är koldioxidneutrala, tillgängliga och uppfyller olika hållbarhetskriterier. En nackdel med biomassa är dock att det innehåller ansenliga mängder föroreningar i form av mineraler som kan frigöras till rökgaserna under förbränning. Frigjorda gaskomponenter kan vara direkt korrosiva via gasfaskorrosion, eller bilda avlagringar på värmeväxlarytor i värmepannans överhettare via kondensation och orsaka avlagringskorrosion. Detta har en negativ effekt på överhettarens livslängd. Alkaliska salter förekommer naturligt och rikligt i biomassa och anses därför ha högst betydelse bland de olika korrosiva föreningarna. Många studier har tidigare gjorts för att förstå mekanismerna i alkali-inducerad korrosion vid höga temperaturer. Dock saknas fortfarande studier för att säkerställa de initiala stegen i korrosionsreaktionen.

I detta arbete presenteras en ny analysmetod som kombinerar kronoamperometri (CA), röntgenfotoelektronspektroskopi (XPS) och svepelektronmikroskopi (SEM). CA har använts för att skapa en tidslinje med korrosionsprocessens inledande mekanismer genom att detektera variationer i elektrisk ström orsakade av redox-reaktioner. XPS och SEM har använts för att studera det bildade oxidskiktets morfologi, tjocklek och sammansättning.

I publikation I-III beskrivs arbetet med att utveckla metoden genom att studera hur de initiala korrosionsmekanismerna påverkas av tre olika alkaliska salter (KCl, NaCl och K_2CO_3). Tester gjordes på Sanicro28 (Fe31Cr27Ni) som är ett vanligt förekommande material i överhettare. Den kombinerade analysmetoden användes för att studera hur katjonerna (K^+ och Na^+) och anjonerna (Cl^- och CO_3^{2-}) påverkar det initiala steget i korrosionsprocessen. Biomassa innehåller, förutom korrosiva salter, även en riklig mängd vatten. Vattenångans inverkan är därför också viktig att ta hänsyn till när man studerar korrosion i förbränning av biomassa, vilket behandlas i publikation IV. För att förstå vattenångans roll i korrosionsmekanismen jämfördes resultat från experiment med fuktig luft och torr luft. I dessa studier observerades att fuktigheten hade en stor inverkan på korrosionen, och därför fokuserade följande delarbete (publikation V) på att mer utförligt studera hur korrosionsmekanismen påverkas av olika syrekällor (vatten/luft). I publikation V användes därför

ytterligare en experimentell metod för att bestämma den detaljerade mekanismen i oxidations-/korrosions-reaktionen; syret i vattnet markerades med den stabila syreisotopen ^{18}O och flygtidssmasspektrometri (Time-of-Flight Secondary Ion Mass Spectrometry – ToF-SIMS) användes för att bestämma källan på syrejonerna i oxidationsreaktionen.

En rad laboratorietester gjordes vid 450 och 535°C där stålet exponerades för alkaliska salter under 2 timmars exponeringstid. Vid båda temperaturerna gjordes observationen att alla tre alkaliska salter påverkade stålet och initierade bildandet av alkalikromat. Den totala korrosionsreaktionens hastighet var betydligt lägre vid 450°C än vid 535°C. Detta stämde för alla tre salter. De bildade kromaterna reagerade vidare till kromoxid med en avsevärt högre reaktionshastighet vid 535°C än vid 450°C, enligt förväntningar.

Det fanns tydliga skillnader mellan katjonernas (K^+ och Na^+) och anjonernas (Cl^- och CO_3^{2-}) påverkan på det initiala steget i korrosionsprocessen. Jämförelse mellan de två katjonerna visade att båda kloridsalterna (KCl och NaCl) hade liknande effekt på ämnesdistributionen i oxidskiktet. Båda salter bidrog till bildandet av alkalikromat, vilket leder till en utarmning av det kromoxidskikt som skyddar det rostfria stålet mot högtemperatur-korrosion. När materialet exponerades för antingen NaCl eller KCl i torr atmosfär gjordes observationen att närvaro av NaCl ledde till en större mängd bildad natriumkromat (Na_2CrO_4) och ett tjockare skikt rikt på krom. Liknande tester i fuktig atmosfär gjordes och jämförelse mellan NaCl och KCl visade att närvaron av NaCl resulterade i en lägre mängd bildad Na_2CrO_4 och att det oxidskikt som bildades var tjockare och mer rikt på järn än det korresponderande skikt som bildades i tester med KCl. Jämförelse mellan anjonerna (Cl^- och CO_3^{2-}) visade att exponering för K_2CO_3 resulterade i en avsevärt större mängd bildad K_2CrO_4 jämfört med exponering för KCl vid tester i torr atmosfär. Tester med K_2CO_3 och KCl i fuktig atmosfär visade att närvaro av K_2CO_3 ledde till bildandet av ett avsevärt tjockare och mer homogent järnoxid-skikt. K_2CO_3 kan sönderfalla och bilda en rad olika intermediära produkter via reaktion med järn, såsom järnbikarbonat ($Fe(HCO_3)_2$).

Resultaten från detta arbete är tänkta att användas i utformning av värmepannor; vid val av material och processparametrar. God förståelse för korrosionsmekanismer behövs för att bättre kunna förutsäga hur material påverkas av de svåra miljöer som uppstår vid förbränning av biomassa.

List of publications

This thesis is based on the following publications given as appendices:

Paper I
The onset of potassium chloride induced high temperature corrosion: A novel experimental approach. **Oxidation of Metals (2014), 82(5-6): 437-456.**

***Jingxin Sui**, Juho Lehmusto, Mikael Bergelin, Mikko Hupa.*

Paper II
Comparison of high-temperature oxidation onset behavior of Sanicro 28 Steel with KCl, NaCl and K_2CO_3. **Solid State Phenomena (2015), 227: 393-396.**

***Jingxin Sui**, Juho Lehmusto, Mikael Bergelin, Mikko Hupa.*

Paper III
The effects of KCl, NaCl and K_2CO_3 on the high-temperature oxidation onset of Sanicro 28 Steel. **Oxidation of Metals (2016), 85(5-6), 565-598.**

***Jingxin Sui**, Juho Lehmusto, Mikael Bergelin, Mikko Hupa.*

Paper IV
Initial oxidation mechanisms of stainless steel Sanicro 28 (35Fe27Cr31Ni) exposed to KCl, NaCl, and K_2CO_3 under dry and humid conditions at 535 °C. **Accepted, Corrosion Science.**

***Jingxin Sui**, Juho Lehmusto, Mikael Bergelin, Leena Hupa.*

Paper V
Applicability of ToF-SIMS and stable oxygen isotopes in KCl-induced corrosion studies at high temperatures. **Corrosion Science (2017), 125, 1-11.**

*Juho Lehmusto, Mikael Bergelin, **Jingxin Sui**, Jyrki Juhanoja, Bengt-Johan Skrifvars, Patrik Yrjas*

Contribution of the author

Papers I-IV. Sui designed the test matrix together with the co-authors, performed the tests, and evaluated the experimental results (CA, XPS and SEM). He was responsible for writing the first draft and finalizing it together with the co-authors.

Paper V. Sui designed the test matrix together with the co-authors, performed the tests, and evaluated some of the XPS results. He was responsible for finalizing the draft together with the co-authors.

Table of contents

Preface ..... **iii**

Abstract ..... **v**

Sammanfattning ..... **vii**

List of publications ..... **ix**

Contribution of the author ..... **x**

1. Introduction **1**

1.1 Purpose of this work 6

2. Literature review **7**

2.1 Corrosion induced by alkali chloride salts 7

2.1.1 Active oxidation 7

2.1.2 Two-stage corrosion mechanism 10

2.1.3 Difference between KCl and NaCl-induced corrosion 14

2.2 Corrosion induced by potassium carbonate 15

2.3 Experimental methods used to study corrosion 16

2.3.1 Surface analysis measurements 16

2.3.2 Electrochemical measurements 17

3. Experimental **19**

3.1 Sample preparation 19

3.1.1 Steel sample preparation 19

3.1.2 Salt pellet preparation 20

3.2 Chronoamperometry (CA) method 20

3.3 Experimental procedures 21

3.3.1 Measurements under stagnant conditions 21

3.3.2 Measurements under flowing conditions 23

3.3.3 Measurements with different oxygen sources 24

3.4 Methods for analyzing the produced reaction layer 25

3.4.1 X-ray photoelectron spectroscopy (XPS) measurements 25

3.4.2 Scanning electron microscope (SEM) measurements 27

3.4.3 Time-of-flight secondary ion mass spectrometry (ToF-SIMS) measurements 27

4. Results and discussion **29**

4.1 Visual observation 29
4.2 CA results 30
4.2.1 Corrosion current under stagnant conditions 30
4.2.2 Corrosion current under flowing conditions 32
4.3 XPS results 34
4.4 Potassium chloride induced corrosion 37
4.4.1 Dry conditions 37
4.4.2 Humid conditions 41
4.4.3 The role of different oxygen sources on the corrosion mechanism 42
4.5 Sodium chloride induced corrosion 44
4.5.1 Dry conditions 44
4.5.2 Humid conditions 47
4.6 Potassium carbonate induced corrosion 48
4.6.1 Dry conditions 48
4.6.2 Humid conditions 51

5. Conclusions 54

6. Future work 57

7. References 58

Original publications 65

1. Introduction

Fossil fuels such as coal, petroleum, and natural gas are non-renewable energy resources, which have been extensively used since James Watt invented the steam engine in 1759. However, various environmental problems have arisen because of the extensive utilization of fossil fuels. For example, burning fossil fuels produces air pollutants, such as nitrogen oxides, sulfur dioxide, volatile organic compounds and gaseous compounds containing heavy metals. In addition, the consumption of fossil fuels has been considered as the primary reason for global warming.

At present, global warming is considered to be one of the most serious global issues. It is caused by the emission of greenhouse gasses (GHG), as GHGs can absorb and emit infrared radiation and consequently they have a warming effect on the climate. The GHGs in the Earth's atmosphere include water vapor (H_2O), carbon dioxide (CO_2), methane (CH_4), nitrous oxide (N_2O) and ozone (O_3). Among these GHGs, CO_2 is the primary GHG which is emitted through human activities[1]. Among the sources of anthropogenic GHG emissions, the use of energy represents by far the largest source of emissions that produce greenhouse gases[2]. It has been reported that CO_2 emissions have increased more rapidly in recent years[3]. Since the Industrial Revolution, human activities have produced an increase of 40% in the concentration of CO_2 in the atmosphere, and particularly the emissions of CO_2 increased at an average rate of 1.9% per year from 1970 to 2015[4].

To solve the challenge with fossil fuels and global warming, alternative energy sources to substitute fossil fuels have drawn much attention. So far, the alternative sources that have been found include nuclear fuels and renewable energy resources (RES). Compared to traditional fossil fuels, the use of RES can effectively decrease the environmental pollution and GHG emissions, especially CO_2 emissions[5]. Since the oil crisis in the 1970s, RES have become more and more popular in energy production. Until 2015, RES contributed with 19.2% of the global final energy consumption[6]. Finland has the 2nd highest share from renewable sources in its gross final consumption of energy in the European Union, which share accounted for 39.3% of the total energy demand in 2015[7].

RES include biomass, hydropower, solar, wind, geothermal, and marine energy sources. Due to the renewability, availability, and various regulatory benefits, biomass represents 75% of the total RES. Currently, biomass accounts for approximately 9% of the total global primary energy demand[6]. The share is especially high in countries with large forest and agricultural resources. Biomass has been considered as a CO_2-neutral fuel because the amount of the released CO_2 during biomass combustion can be accumulated through photosynthesis during plant growth. Only a relatively small amount of fossil energy used in cultivation and transportation of biomass contributes to a net atmospheric CO_2-increase. Biomass includes a large variety of fuels with different chemical composition and combustion characteristics. The components of biomass include cellulose, hemicelluloses, lignin, extractives, lipids, proteins, simple sugars, starches, water, ash, and other compounds[8]. Compared to coal, biomass contains less C, more H and O, more Cl, Si and K, less S, Al and Fe. Further, it has lower heating value (HV) and higher moisture content[8].

Biomass has been widely used as an energy source either directly via combustion to produce heat, or indirectly through conversion into various forms of biofuel[9]. In Finland, biomass is used directly as a fuel for burning or cofiring with traditional fossil fuels in electricity generation, combined heat and power (CHP) plants and district heating. In fact, Finland is among the world leaders in the use of CHP: the largest user of biomass for energy production in Europe, and the second biggest producer of CHP electricity in Europe (Denmark is the 1st)[10]. In addition, the CHP plants in Finland have the best thermal efficiency of averagely 83%[10]. A schematic picture of a typical biomass boiler in a CHP plant is shown in Figure 1. For the sustainable approach to forest/biomass resources in Finland, Finnish managed forestry has maintained a consistently growing biomass stock in the forests over the last 50 years. Sustainable forest management in Finland has roots in the 17th century and was first codified in the Forest Act of 1886. The principles of ecological, social and economic sustainability are laid out in the Forest Act of 1996. Nowadays, a planning tool, MELA, was used by the Natural Resources Institute in Finland to calculate the maximum amount of allowable woodcuts each year are established.

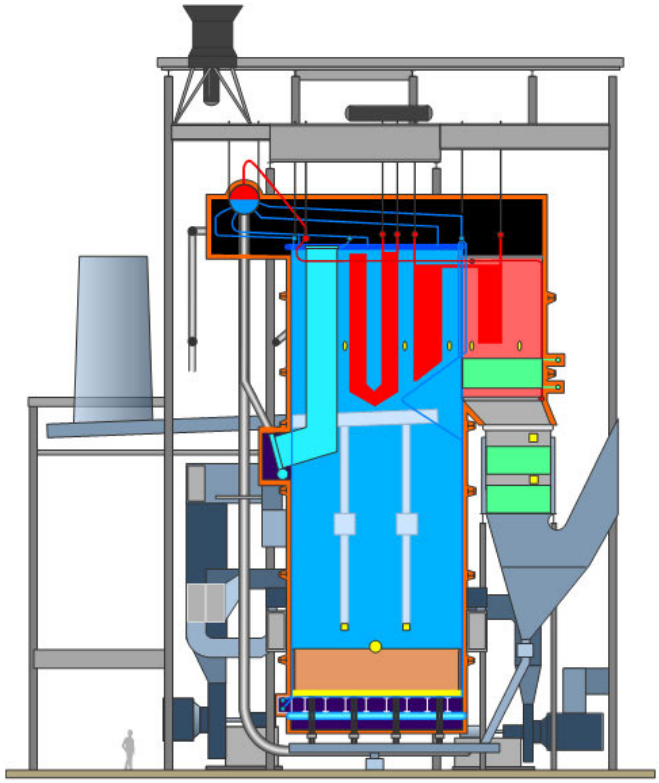

Figure 1. A schematic picture of a biomass combustion boiler (Courtesy of Valmet Technologies)

Burning or cofiring biomass is not free of challenges. Compared to coal combustion, the use of biomass as a fuel has turned out to be challenging due to its high moisture and the composition of the ash[11,12]. For instance, some types of biomass like wood have a very little ash fraction and seldom cause any trouble in boilers, whereas some other biomasses such as straw, grass and wood residues contain problematic elements, mainly alkali metals (K and Na) and chlorine (Cl), in such a form that they form deposits and ashes with low eutectic temperatures during the combustion process[13–18]. If the temperature at the material surface is higher than the melting point of these deposits, the formed molten phase has an accelerating effect on the corrosion of the superheater tube materials. The molten phase formed may provide an electrolyte or ionic transfer pathway for the electrochemical attack. The corrosion is thus promoted in the molten phase, rendering it particularly hazardous for the superheater tubes[19]. In commercial biomass combustion plants, a

common way to avoid the molten phase corrosion and to decrease the rate of the high temperature corrosion is to limit the material surface temperature below the melting point of the corrosive salts by lowering the steam temperature. However, although limiting the steam temperature decreases the corrosion rate, it also decreases the power generation efficiency. Furthermore, alkali chloride-induced corrosion can accelerate the corrosion process also at temperatures well below 400 °C[20]. In order to find better solutions for the corrosion problems, a thorough understanding of the corrosion mechanism and factors that affect the corrosion process is vital. Among the corrosive salts, potassium chloride (KCl) is commonly considered as the most challenging corrosive species because it exists naturally and extensively in various biomasses[13]. KCl-induced high-temperature corrosion has been extensively studied, and several hypotheses for the corrosion mechanism have been proposed[11,13–15,17]. Another corrosive alkali chloride salt, NaCl, exists in some special fuel fractions, such as in recovered waste wood and in floated logs, which have absorbed sea water[21]. When cofiring coal and biomass, a small quantity of NaCl also forms together with the formation of sulfates. The corrosive effect of NaCl has been compared with KCl by several research groups[21–24]. Compared with chloride salts, carbonate salts have a much lower concentration in the biomass ash deposit. K_2CO_3 has been found as a corrosive compound in fly ash in the biomass combustion process[25]. Similar to KCl, K_2CO_3 can also react with the passivation oxide layer of the superheater tubes and forms potassium chromate, leading to the degradation of the tube materials. The hypotheses of the corrosion mechanisms by these three alkali salts will be summarized and discussed in the next chapter.

To minimize the corrosion damage during the combustion of biomass, the boiler material is a very important factor to take into account. In particular, the choice of superheater tube material is important as the superheater are subjected to the highest temperatures tubes inside a biomass boiler[26]. The performance of a metal at elevated temperatures is typically controlled by the protective qualities of the oxide that forms on the surface of the metal. The most common method to prevent or slow down corrosion is to use chromium-rich stainless steels as a superheater material. Chromium forms a protective layer consisting of pure chromium oxide, corundum-type binary oxide ($(Fe,Cr)_2O_3$), or iron chromium spinel-type oxide ($FeCr_2O_4$) on the surface of the steel

depending on alloying elements and their relative ratios in the steel[27–29]. The protective oxide layer prevents surface corrosion by hindering oxygen and other corrosive species from diffusing further into the bulk steel, given that the protective layer remains intact. In previous research, several chromium containing commercial stainless steel types have been studied in corrosive environments. These steels include 10CrMo9-10, steel T91, 304L steel, Sanicro 28 and Alloy 625[29–31]. It is generally known that only increasing the chromium content in the steel is not always a remedy against alkali salt-induced corrosion. At temperatures relevant to biomass combustion (400 °C–600 °C), the protective oxide layer can be affected by the alkali salts present in the flue gases. These alkali salts react with the chromium oxide and hence destroy the protective layer. Consequently, it is anticipated that these interactions might result in accelerated corrosion of the underlying alloy. To further improve corrosion resistance, some other corrosion resistant alloy elements such as nickel, molybdenum could be added in the steel. Nickel helps to form austenitic crystal structures, which improve the properties such as plasticity, weldability, strength and toughness. Nickel also greatly improves resistance to oxidation and corrosion. Molybdenum increases the high-temperature strength of the steel, such as long-lasting and creep properties, and also improves resistance to pitting and crevice corrosion especially in chloride and sulfur containing environments[27]. Sanicro 28, a high alloy stainless steel, has high chromium contents, high nickel contents and 3.5% molybdenum. It has been widely studied and used as superheater material in Europe due to its high resistance to corrosion and relatively good ductility[32]. The high chromium content of Sanicro 28 contributes to high gas corrosion resistance. Sanicro 28 is typically used as superheater tube material in various steam boiler applications such as black liquor recovery, municipal refuse and biomass boilers. Sanicro 28 has a homogenous passivation oxide layer on the surface, which mainly consists of corundum-type binary oxide ($(Fe,Cr)_2O_3$). Some iron chromium spinel-type oxide ($FeCr_2O_4$) may also exist as defects in the passivation layer. This spinel-type oxide has the low activation energy and easily reacts with corrosive species[33,34]. In this work, Sanicro 28 has been chosen as the main material to be investigated in papers I-V. In paper V, a low alloy stainless steel 10CrMo9-10 and a nickel-based austenitic stainless Alloy 625 were investigated in addition to Sanicro 28.

1.1 Purpose of this work

This thesis focuses on using new tools to measure and understand the mechanism of the initial stages of the alkali salts induced corrosion of the superheater materials. In this work, Sanicro 28 was used as the main substrate. In particular, the following topics were addressed:

1. To give an increasing understanding of the high temperature corrosion mechanisms in stagnant conditions, a novel combinatory method of chronoamperometry (CA), X-ray photoelectron spectroscopy (XPS) and scanning electron microscopy (SEM) were used to give an insight into the early stages of the oxide layer degradation of Sanicro 28 in the presence of KCl. The results of this topic were presented in Paper I.

2. The corrosion effects of three alkali salts, KCl, NaCl and K_2CO_3, were studied by the combinatory method to analyze the onset corrosion mechanisms of Sanicro 28. The role of the cations (K^+ and Na^+) and anions (Cl^- and CO_3^{2-}) on the onset of the corrosion process were compared under stagnant conditions. The results of this topic were presented in Papers II and III.

3. The combinatory method was modified to illustrate the roles of the cations (K^+ and Na^+) and anions (Cl^- and CO_3^{2-}) in the onset of corrosion mechanism of Sanicro 28 in the presence of humidity. The role of the water vapor in the onset of the corrosion process was also discussed. The results of this topic were presented in Papers IV.

4. As the effect of the water vapor is discussed and highlighted, the stable oxygen ^{16}O and ^{18}O isotopes were introduced in combination with ToF-SIMS to increase the understanding of the corrosion mechanism under conditions where multiple oxygen sources (atmospheric oxygen and water vapor) were present. In this topic, low alloy stainless steel 10CrMo9-10 and nickel-based alloy 625 in comparisons with Sanicro 28 were discussed. The results of this topic were presented in Papers V.

2. Literature review

In the literature review, KCl, NaCl and K_2CO_3 induced corrosion mechanisms proposed by the previous research are summarized and discussed. This chapter is divided into three subchapters. Chapter 2.1 describes the previous research on the alkali chlorides induced corrosion and Chapter 2.2 describes the effect of K_2CO_3. Chapter 2.3 summarizes previous experimental methods including some surface analysis methods in 2.3.1 and electrochemical methods in 2.3.2.

2.1 Corrosion induced by alkali chloride salts

In the biomass combustion process, alkali chloride salts in the sticky deposits are aggressive species that cause severe corrosion of the superheater tubes. Molten salts in the deposit cause the most severe corrosion attack[20].

Many research groups have investigated the mechanisms involved in alkali chloride induced high temperature corrosion, and several hypotheses have been proposed. One hypothesis called 'active oxidation' was used to explain the long-term corrosion process[35,36]. However, this hypothesis does not fully explain the fast reactions at the initial stage of the corrosion process especially at lower temperatures where only solid/solid interactions are available. Recently, a two-stage corrosion mechanism hypothesis has been proposed, intended to explain the initial corrosion reaction[31].

2.1.1 Active oxidation

The term 'active oxidation' was first proposed by Lee and McNallan in 1987[35], who studied the corrosion reaction between pure nickel and NaCl. Nowadays, this term refers to the direct acceleration of the oxidation of the metal alloys by the gases or deposits containing Cl_2, HCl, NaCl, KCl, etc. Based on the thermodynamic fundamentals and experimental observations, Grabke et al.[36] have given the basic understanding of the active oxidation mechanism of low alloy steel by describing the chemical reactions involved in the process. The main reactions involved in the active oxidation mechanism have been summarized as follows (Eqs. 1 – 7)[36]. The equations were presented without specifying the state symbols. The present author has inferred them to the best of his ability:

$$2HCl\ (g) + 1/2\ O_2\ (g) \rightarrow Cl_2\ (g) + H_2O\ (g) \quad (1)$$

$$2NaCl\ (s) + Fe_2O_3\ (s) + 1/2\ O_2\ (g) \rightarrow Na_2Fe_2O_4\ (s) + Cl_2\ (g) \quad (2)$$

$$4NaCl\ (s) + Cr_2O_3\ (s) + 5/2\ O_2\ (g) \rightarrow 2Na_2CrO_4\ (s) + 2Cl_2\ (g) \quad (3)$$

$$Fe\ (s) + Cl_2\ (g) \rightarrow FeCl_2\ (s) \quad (4)$$

$$FeCl_2\ (s) \rightarrow FeCl_2\ (g) \quad (5)$$

$$3FeCl_2\ (g) + 2O_2\ (g) \rightarrow Fe_3O_4\ (s) + 3Cl_2\ (g) \quad (6)$$

$$2FeCl_2\ (g) + 3/2\ O_2\ (g) \rightarrow Fe_2O_3\ (s) + 2Cl_2\ (g) \quad (7)$$

The active oxidation starts with the formation of molecular chlorine from the oxidation of HCl (Eq. 1) or from condensed chlorides (Eqs. 2, 3). The formed chlorine can penetrate the oxide layer through pores or cracks and reacts with the bulk material to form gaseous transition iron chlorides, where the partial pressure of oxygen is low. At the elevated temperatures in the (biomass) boilers, a continuous evaporation of these iron chlorides will take place and leads to a considerable vapor pressure at the metal/oxide interface (Eq. 4, 5). Consequently, these volatile chlorides will diffuse outward through cracks and pores of the oxide layer to the areas with higher partial pressures of oxygen, where they may react with oxygen, forming Fe_3O_4 and/or Fe_2O_3 while releasing molecular chlorine (Eqs. 6, 7). Part of the released molecular chlorine can again diffuse towards the metal surface, and thus sustain the oxidation of the metallic surface beneath the non-protective oxide layer. Eventually, the net reactions (Eqs. 4–7) form a cycle where a continuous transport of metal occurs at the metal/oxide interface toward the higher oxygen partial pressure in the bulk gas. These reactions can collectively be defined as the 'chlorine cycle' mechanism, where Cl_2 plays a seminal role by acting as a catalyst in the corrosion process. This process depletes the protective layer of chromium and tends to convert it to a poorly protective iron oxide layer which provides no passivating protection against further corrosion[36].

The validity of the active oxidation mechanism has been experimentally verified in several studies[14,18,31,37–44]. In particular, the corrosion of iron, chromium, nickel and their alloys in the presence of Cl_2, HCl, NaCl, or KCl has been examined at temperatures ranging from 400 °C to 700 °C. The KCl-induced corrosion of stainless steel has been evaluated mostly

in conditions typical for the superheater tube materials. These studies have been conducted both in lab-scale and in large scale via variable temperature and humidity conditions to summarize the corrosion reactions of high alloy FeCrNi stainless steels. Under dry conditions and at temperatures above 450 °C, KCl initially reacts with the protective oxide layer on the surface of the stainless steel to form potassium chromate and chlorine gas (Eq. 8), resulting in a chromium-depleted non-protective oxide layer[31]. After this initial reaction, chlorine can penetrate through the oxide layer and react with the bulk material to form volatile metal chlorides (Eqs. 9, 10). These volatile metal chlorides then convert to oxides and form Cl_2 when they diffuse back to the steel surface where the partial pressure of oxygen is higher (Eq. 11). Part of the released Cl_2 can diffuse back towards the metal surface, reinforcing the process and recycling the reactions (Eqs. 9–11)[14]. Through the series of reactions, a porous non-protective oxide is formed at the alloy surface, and further material degradation will occur.

$$\mathbf{Cr_2O_3\,(s) + 4KCl\,(s) + (5/2)O_2\,(g) \rightarrow 2K_2CrO_4\,(s) + 2Cl_2\,(g)} \quad \mathbf{(8)}$$

$$\mathbf{M\,(s) + Cl_2\,(g) \rightarrow MCl_2\,(s)} \quad \mathbf{(9)}$$

$$\mathbf{MCl_2\,(s) \rightarrow MCl_2\,(g)} \quad \mathbf{(10)}$$

$$\mathbf{4MCl_2\,(g) + 3O_2\,(g) \rightarrow 2M_2O_3\,(s) + 4Cl_2\,(g)} \quad \mathbf{(11)}$$

where M = Fe, Cr, Ni.

In contrast to the dry ambient conditions described above, the water content in the biomass fuel is usually high, and consequently, the effect of water vapor cannot be ignored when studying the corrosion process during biomass combustion. The major difference between reactions in dry conditions and wet conditions lies in the formation of thermodynamically stable HCl under wet conditions rather than Cl_2, which forms under dry conditions at the initial stage. HCl, in turn, contributes to the synergistic corrosion accelerating the effect of water vapor[31]. The initial reaction can be simplified to Eq. 12[31]:

$$\mathbf{Cr_2O_3\,(s) + 4KCl\,(s) + 2H_2O\,(g) + (3/2)O_2\,(g) \rightarrow 2K_2CrO_4\,(s) + 4HCl\,(g)} \quad \mathbf{(12)}$$

After this initial reaction, the formed HCl is also able to diffuse and chlorinate the alloying metal from bulk material, resulting in the formation of volatile metal chlorides. These metal chlorides may diffuse

back to the metal/oxide interface and react with oxygen and water vapor, yielding a porous oxide and regenerating HCl, which reinitiates the chlorination reaction in a cyclic manner (Eqs. 13, 14)[14]:

$$\mathbf{M\,(s) + 2HCl\,(g) \rightarrow MCl_2\,(g) + H_2\,(g)} \quad \textbf{(13)}$$

$$\mathbf{4MCl_2\,(g) + 4H_2O\,(g) + O_2\,(g) \rightarrow 2M_2O_3\,(s) + 8HCl\,(g)} \quad \textbf{(14)}$$

where M = Fe, Cr, Ni.

2.1.2 Two-stage corrosion mechanism

Although the 'active oxidation' has been proven to describe the long-term corrosion process fairly well, there are still a lot of doubts about whether this oxidation mechanism is also valid for the initial corrosion stage. One key question is how the molecular chlorine diffuses or penetrates into the metal/oxide interface in the initial reaction stage[14]. According to Grabke et al.[36], the chlorine itself pushes its way through the oxide by cracking, grain boundary grooving or fissuring. However, it is under debate if these mechanisms are rapid enough to explain the immediate start of corrosion reactions after the introduction of the chloride component. Moreover, regarding active oxidation, molecular chlorine is expected to diffuse inward forming metal chlorides when the oxygen partial pressure is low. These formed metal chlorides are volatile and can diffuse outward through the oxide layer until they get in contact with molecular oxygen and form an oxide and chlorine. The follow-up questions are then: Why not the smaller molecular oxygen but only chlorine diffuses through the oxide layer? What is the driving force for the diffusion of the formed chloride species[14]?

With these issues, Pettersson et al. proposed a new two-stage corrosion mechanism to explain the initial corrosion stage[31,45,46]. This mechanism divided the initial corrosion reaction into two continuous stages. Firstly, alkali cations react and break down the protective passivation layer. The alkali chromate crystals and gaseous chloride species (Cl_2 or HCl) form in this reaction. Secondly, the chloride species (mainly chloride ions) can penetrate or diffuse into the oxide layer and react with the metal underneath. This two-stage corrosion mechanism hypothesis will be discussed below.

According to the two-stage corrosion mechanism hypothesis, alkali cations in alkali chlorides play a fundamental role in the initial corrosion process. In the first stage, potassium or sodium cations react with the protective passivation oxide layer to form alkali chromate crystals and release hydrogen chloride or molecular chlorine. The chemical reaction of this stage is schematically similar to the one in active oxidation mechanism in Eqs. 8 and 12. However, the theory behind these two mechanisms is different. In the first step of the active oxidation mechanism, the emphasis is put on the formation of chloride species, which further react with the steel and take part in the chlorine cycle. In the two-stage corrosion mechanism, the emphasis is put on the formation of the alkali chromate crystals, which can be considered as a sink for the chromium oxide passivation layer. Potassium chromate formation destroys the protective oxide by depleting it in chromium and resulting in breakaway corrosion. Accordingly, the protective layer of chromium is converted to a less protective iron oxide layer, which provides a suitable pathway for the second stage to proceed.

The formation of alkali chromate crystals has been proposed in previous research. Shinata et al. first proposed the formation of sodium chromate by studying the effect of NaCl on pure chromium, Cr–Ni alloys and stainless steel[23]. In their results, it was found that the presence of NaCl accelerated the oxidation of stainless steels, especially the high alloy stainless steel containing a high content of chromium. Shinata et al. also proposed that NaCl reacts with the stainless steel, resulting in a non-protective Cr_2O_3 film containing Na_2CrO_4. Further, a eutectic melt between NaCl and Na_2CrO_4 formed when the quantity of NaCl was high[23]. However, the formation of Na_2CrO_4 did not get attention as an important intermediate but was at that time only considered as a species participating in the reaction[23].

The role of cations has been discussed in several articles as well. Shinata et al.[23] compared several chloride salts to study the role of different cations such as Na^+, NH_4^+ and Ni^{2+}. According to their findings, Cl^- anion plays a primary role in the corrosion process, and the studied cations only affect the magnitude of the acceleration rate. Lehmusto et al.[47] attempted to elaborate the impacts of chlorides in the corrosion mechanisms by investigating the effect of eight different chlorides ($BaCl_2$, $CaCl_2$, KCl, LiCl, $MgCl_2$, NaCl, $PbCl_2$ and $ZnCl_2$) with pure metallic

chromium powder under dry conditions in four different temperatures (400, 500, 550, and 600 °C) in the two-hour reaction time. According to their findings, $BaCl_2$, $CaCl_2$ and $MgCl_2$ did not react with chromium even at 600 °C, whereas $ZnCl_2$ evaporated already before the reaction started. KCl, NaCl and $PbCl_2$ reacted at 500 °C and higher temperatures, and LiCl reacted only at 600 °C. They concluded that the presence of chlorine does not sufficiently explain the accelerated initiation of oxidation, and thus their work supported the role of the cations in the initial corrosion stage.

According to the two-stage corrosion mechanism, the formation of alkali chromates first destroys the protective chromium oxide layer on stainless steels, after which gaseous chloride species (Cl_2 or HCl) will diffuse through the oxide and react with metal at the metal/oxide interface. One fundamental problem in the active oxidation mechanism theory is that the corrosion reaction rate is limited by the diffusion of molecular chlorine or hydrogen chloride through the oxide layer. As an explanation, Pettersson et al. suggested that chlorine penetrates the layer as grain boundary diffusion of chloride ions in the initial corrosion stage[32]. Several research groups have thereafter focused on explaining the diffusion of the chloride species[45,48,49].

Firstly, Jonsson et al. presented an ESEM in situ investigations of initial stages of the KCl-induced high temperature corrosion of low alloy steel (Fe-2.25Cr-1Mo) at 400 °C[45]. In their work, it was found that a large area of the sample surface was covered by much thicker corrosion products after only one hour of exposure to KCl than in the absence of KCl. The authors claimed that the fast reaction in the first hour is attributed to the diffusion of Cl^- anions.

Then, Folkeson et al. repeated the experiments by Jonsson et al. but in the ambient gas flow at 400 °C and 500 °C[48]. In the flow gas condition, the formed HCl or Cl_2 was supposed to be sufficiently diluted and transported away from the sample. Thus, the gaseous HCl and Cl_2 can be eliminated from the main sources of the chloride containing species. They found that the oxidation rate was still accelerated and iron chloride accumulated at the metal/oxide interface after short exposure times, in the absence of gaseous chlorine species. The observation of the formed iron chloride indicates that chlorine transported through the oxide layer in the form of chloride ions rather than molecular chlorine. The reason for the diffusion of chlorine species rather than molecular oxygen was

assumed to depend on the lower charge/radius of chloride ion than oxygen ion, thus providing a higher mobility on an oxide surface and in the grain boundary region of the oxide layer. Based on the experimental observations, Folkeson et al. proposed a new electrochemical mechanism to explain the diffusion of chloride anions and their interactions with the metal at the initial corrosion stage, which is summarized below (Eqs. 15–18)[48].

$$\mathbf{Fe \rightarrow Fe^{2+} + 2e^{-}} \quad \textbf{(15)}$$

$$\mathbf{O_2 + 4e^{-} \rightarrow 2O^{2-}} \quad \textbf{(16)}$$

$$\mathbf{2KCl + 1/2O_2 + H_2O + 2e^{-} \rightarrow 2KOH(ads) + 2Cl^{-}(ads)} \quad \textbf{(17)}$$

$$\mathbf{Fe^{2+} + 2Cl^{-} \rightarrow FeCl_2(s)} \quad \textbf{(18)}$$

In the absence of KCl, iron is oxidized to Fe^{2+} ions at the metal/oxide interface, and oxygen is reduced on the surface (Eqs. 15, 16). There is an electric current running from the alloy to the oxide surface and a corresponding ionic current, resulting in the growth of the oxide layer. In the presence of KCl and water vapor, iron is still oxidized to Fe^{2+} ions at the metal/oxide interface (Eq. 15), whereas oxygen is reduced on the oxide layer surface resulting in potassium hydroxide and chloride ions (Eq. 17). The chloride ions are apt to diffuse towards the metal due to the chloride concentration gradient. Oxide grain boundaries provide feasible paths for the diffusion of chloride ions to the metal surface. Iron chloride forms when the chloride ions encounter iron ions (Eq. 18). The fact that iron chloride is found at the bulk metal/oxide layer interface suggests that the inward diffusion of chloride ions is fast.

Another series of studies have been done by Israelsson et al., who studied KCl-induced corrosion of a FeCrAl alloy (Kanthal)[38,49–51]. In their work, the initial reaction was defined as a cathodic process on the layer surface, generating 'free' chloride ions and incorporating potassium in a stable form. The authors claimed that the reaction is validated both in the case of FeCrNi and FeCrAl alloys in the presence of KCl, O_2 and H_2O, which shows that potassium chromate formed on the corroding metal surface according to Eq. 15 and 19:

$$\mathbf{2KCl + 5/4O_2 + 1/2Cr_2O_3 + 2e^{-} \rightarrow K_2CrO_4 + 2Cl^{-}} \quad \textbf{(19)}$$

Israelsson's findings support the results by Folkeson et al.[48] and thereby give basis for an electrochemical mechanism, which contributes to the understanding of the fast chloride diffusion process in the initial alkali chloride-induced corrosion of high alloy steels.

2.1.3 Difference between KCl and NaCl-induced corrosion

Both KCl and NaCl have been reported in the literature to remarkably accelerate the oxidation of stainless steels[21]. KCl or NaCl can trigger the breakdown of the protective oxide layer by the formation of K_2CrO_4 or Na_2CrO_4 and result in a thick layer consisting of an outer hematite layer and an underlying spinel-type oxide on the stainless steel surface. In this chapter, previous studies about the corrosion effect of KCl and NaCl are summarized.

Enestam et al. compared the corrosion effect of KCl and NaCl on several stainless steels under the experimental conditions at 400–650 °C in the ambient air[21]. They found out that even though there were some differences between these two salts regarding their corrosive effect in the grain boundaries, they were considered equally corrosive on the tested stainless steels (10CrMo9-10, AISI347). The major differences in the corrosive effects of NaCl and KCl were observed on Sanicro 28 steel. In the presence of NaCl, the corrosion product layer on Sanicro 28 was roughly twice as thick as that formed in the presence of KCl for 168h (1 week) exposure time.

In contrast, Lehmusto et al.[25] showed that both NaCl and KCl increase the oxidation of metallic chromium and form porous Cr_2O_3 consisting of separate crystals at temperatures above 500 °C. Nevertheless, the oxidation rate of chromium at 600 °C was higher in the presence of KCl than in the presence of NaCl regarding the relative mass change and the average size of the formed crystal.

According to the work by Karlsson et al.[22], the rate of corrosion attack is different for samples exposed to NaCl and KCl. It was observed that the amount of Na_2CrO_4 formed was higher than K_2CrO_4, as K_2CrO_4 was not stable and decomposed with time. Additionally, the samples exposed to NaCl contained not only Na_2CrO_4 but also a corrosion product containing Na, Fe and O, possibly $Na_2Fe_2O_4$. In contrast, the samples exposed to KCl contained only K_2CrO_4. The authors claimed that the

differences in the corrosion process are attributed to the greater volatility of KOH than that of NaOH.

Recently, six chloride salts were compared by Liu et al. to elucidate the impacts of chlorides at 500 °C for 1000 h[52]. The authors suggested that, based on the mass-loss data, the corrosivity of the studied metal chlorides increase in the order $CaCl_2 < NaCl < KCl < ZnCl_2 < PbCl_2 < FeCl_2$. They claimed that the reason for the different corrosion behavior is because materials exposed to chloride salts corrode through vicious cycles, in which a shorter path of the cycle leads to a higher corrosion rate. By the investigation of the corrosion effect of KCl and NaCl on six superheater tube materials, they claimed that the corrosivity of KCl is higher than that of NaCl due to the higher volatilization rate of KCl.

Based on the previous work, it can be concluded that both KCl and NaCl are corrosive in the typical condition of a biomass boiler, and that there are some differences between the corrosion effects.

2.2 Corrosion induced by potassium carbonate

Potassium carbonate (K_2CO_3), which is frequently found in the fly ash, has also been recognized as a corrosive substance in biomass combustion[53]. In this chapter, differences in the corrosion effect of KCl and K_2CO_3 are summarized.

Pettersson et al. studied the corrosion effect of KCl and K_2CO_3 on 304-type (Fe18Cr10Ni) austenitic stainless steel. They found that both KCl and K_2CO_3 can cause chromium depletion of the protective oxide which results in the formation of a thick duplex layer containing an outer hematite layer and an inner layer consisting of FeCrNi spinel-type oxide[54]. For longer exposure times (>24 h), the oxide layers, which form in the presence of K_2CO_3 and KCl are different. In the presence of K_2CO_3, the formed oxide layer is homogeneous and firmly adhered to the sample surface, whereas in the presence of KCl, the formed oxide layer is thicker and consists of multiple layers which are apt to be detached from the sample surface. The different corrosion effect of K_2CO_3 compared to KCl might be due to the lack of mobile intermediates like metal chlorides, which only formed in the alkali chloride-induced corrosion[55].

In a series of articles by Lehmusto et al., the corrosivity of K_2CO_3 was compared with KCl by utilizing pure chromium and three stainless steels[25,53,56]. K_2CO_3 did not react with pure chromium but could react with chromium oxide and Cr_2O_3-protected stainless steels to form potassium chromate. They proposed that, ideally, the K_2CO_3-induced corrosion reaction is initiated by the destruction of this passive layer upon the activity of potassium ion with the formation of K_2CrO_4 and/or potassium dichromate ($K_2Cr_2O_7$). They suggested the corrosion reaction in the presence of K_2CO_3 as follows (Eqs. 20–21):

$$\mathbf{K_2CO_3\,(s) + Cr_2O_3\,(s) + 3/2\ O_2\,(g) \rightarrow K_2Cr_2O_7\,(l) + CO_2\,(g)} \quad \textbf{(20)}$$

$$\mathbf{4K_2CO_3\,(s) + 2Cr_2O_3\,(s) + 3\ O_2\,(g) \rightarrow 4K_2CrO_4\,(s) + CO_2\,(g)} \quad \textbf{(21)}$$

After the initial reaction, the oxidation reaction does not proceed further, and the authors claimed that the reason might be due to the lack of mobile intermediates[25]. This is in accordance with the statement of Pettersson et al.[54]

Lehmusto et al. also discussed the effect of water vapor on the potassium carbonate induced corrosion to simulate a realistic environment for biomass combustion processes[25]. They claimed that the main impact of humidity was an increase in the oxide layer thickness in comparison with the case under dry conditions, whereas the oxide structure was not significantly affected.

2.3 Experimental methods used to study corrosion

2.3.1 Surface analysis measurements

In the previous chapters, the mechanisms of alkali salts-induced corrosion under dry and wet conditions were summerised[14,15,17,55-59]. In these studies, various analytical methods have been utilized to implement the tests[57]. For instance, steel coupon exposure tests and thermogravimetry have been used to study reaction kinetics[58,59]. X-ray diffraction (XRD) and mass change measurements have been used to analyze the crystalline corrosion products and consequently to study the oxide layer conversion[56]. Ion chromatography (IC) has been used to detect the formation of chromate[46]. Spectroscopic characterization techniques, such as scanning electron microscopy (SEM) and transmission electron microscopy (TEM) combined with energy-

dispersive X-ray analysis (EDX), have been used to study the surface morphology and to identify the crystalline components[38,60]. Atomic emission spectroscopy (AES) and X-ray photoelectron spectroscopy (XPS) have been used to identify and measure the chemical state of the elements within the oxide layer[45,49]. Secondary ion mass spectrometry (SIMS) has been used to analyze the composition of solid surfaces and thin films to identify the isotopes of certain elements within surface layer[61]. Most of these methods have been tested in this work. However, due to the short exposure time studied for the initial stage mechanisms and relative low amount of the corrosion products formed during the tests, only SEM-EDX, XPS, ToF-SIMS were selected to be combined with online electrochemical measurement and detection of the corrosion reactions.

2.3.2 Electrochemical measurements

As corrosion is an electrochemical process, a number of electrochemical techniques have been employed to analyze the corrosion mechanism at both room temperature and high temperatures. The majority of the electrochemical experiments have been conducted at room temperature in the range of 20–25 °C. In these low temperatures experiments, several different electrochemical parameters have been utilized to study the corrosion mechanisms. These parameters include standard electrode potentials, activity coefficients, conductance measurements, equilibrium constants, diffusion activation constants, electrodeposition of metals and alloys, a variation of electrocapillary maxima and points of zero charge[62–66]. Several electrochemistry studies of molten salt corrosion have been published of the corrosion at elevated temperatures. Methods that have been used include electrochemical noise (EN), electrochemical impedance spectroscopy (EIS), free corrosion potential, scanning polarization, cyclic voltammetry, potentiostatic polarization, and linear polarization[24,67–75].

Among these techniques, EIS and EN are the most popular methods for the understanding of the corrosion process at elevated temperature. EIS has been widely used in the study of aqueous corrosion and it has proved to be effective in understanding reaction mechanisms and kinetics[70–72]. The advantage of EIS is that it provides information on the kinetics of the reaction process and changes in the state of the electrode surface. Thus, EIS has been utilized to the research of corrosion inhibitor

adsorption on the surface of corroded metal electrodes under high temperature and high pressure[76], and the study of the surface film or coating of high temperature materials[77]. EN could reflect the potential and the externally measured current in an electrochemical system, which has been employed for providing fundamental information of corrosion processed and for evaluating the performance of the coatings against corrosion[73–75]. However, the signal levels obtained with EIS and EN are very low and prone to interference from induction currents due to heating elements switch on/off when measurements are conducted in oven surroundings. In order to obtain the electrochemical information from the corrosion reaction apart from the surroundings, a tailored 2-electrode chronoamperometry (CA) method has been proposed and utilized in this work.

3. Experimental

This chapter is a summary of the experimental part of Papers I – V. All the experimental parameters are described in detail in the attached original papers. Paper I introduced the novel experimental setup to study the corrosion effect of KCl, and Papers II to IV utilized this novel experimental setup to study the corrosion mechanism induced by different alkali salts. Paper V utilized Time-of-Flight Secondary Ion Mass Spectrometry (ToF-SIMS) to identify the stable oxygen isotopes (^{16}O and ^{18}O) used to label the oxygen sources in the high-temperature corrosion tests.

3.1 Sample preparation

3.1.1 Steel sample preparation

Austenitic stainless steel Sanicro 28 (Table 1) samples cut into rectangular pieces (20 × 20 × 10 mm^3) were used as working electrode (Paper I-IV) and counter/reference electrode (Paper IV), whereas Sanicro 28 cylindrical pieces (diameter 12 mm, thickness 10 mm) were used as counter/reference electrode (Paper I-III). Stainless steel wires were welded to the steel samples to provide an electric contact with the potentiostat for the chronoamperometry (CA) measurements. In Paper V, 10CrMo9-10, Sanicro 28 and Alloy 625 were cut into rectangular pieces of the size (20 × 20 × 10 mm^3) (Table 1). Before the experiments, all the samples were polished with Grit500/ P1000 SiC grinding paper to remove the scratches and to obtain a reproducible even surface roughness. After polishing, the samples were cleaned with ethanol, and pre-oxidized for 24 hours at 200 °C in stagnant ambient air to ensure a reproducible oxide layer at the surface.

Table 1. The nominal chemical compositions of the studied alloys in wt%. (Papers I-V)

Alloy	10CrMo9-10	Sanicro 28	Alloy 625
Cr	2.0-2.5	27.0	20.0-23.0
Fe	Balance	Balance	5.0
Ni	--	31.0	Balance
Mn	0.4-0.8	≤ 2.0	0.5
Mo	0.9-1.1	3.5	8.0-10.0
Si	≤ 0.5	≤ 0.6	≤ 0.5
C	0.08-0.14	≤ 0.02	≤ 0.1
Cu	≤ 0.3	1.0	--
P	≤ 0.03	≤ 0.025	≤ 0.015
S	≤ 0.025	≤ 0.01	≤ 0.015
Co	--	--	≤ 1.0
Nb+Tb	--	--	3.15-4.15
Al	--	--	≤ 0.4
Ti	--	--	≤ 0.4

3.1.2 Salt pellet preparation

The salts under investigation were pro analysis-grade potassium chloride, potassium carbonate, potassium sulfate and sodium chloride [Merck]. Before the measurements, the salts were dried at 120 °C, ground and sieved. The size fraction 50–100 μm particles were used to manufacture the salt pellets used for the corrosion tests. The salt pellets were pressed to give pellets with the diameter 8 mm and thickness 2 mm by applying a pressure of 2000 kg/cm^2. After pressing, the pellets were stored in a desiccator to minimize the risk of moisture contamination before the measurements. Steel sample pre-treatment, density and thickness of the salt pellets, as well as reaction quenching were standardized to ensure high reproducibility in both the CA measurements and surface analyses.

3.2 Chronoamperometry (CA) method

CA measurements have commonly been used to determine conversion rate and the amount of material converted in electrochemical reactions at room temperature. This approach does not render itself useful in cases where substantial simultaneous oxidation and reduction reactions occur. As only the net current from these reactions can be detected, the value of CA as a quantitative method is severely limited. However, the relative magnitude, shape and growth rate of the CA current gives qualitative information of the onset and reaction transitions in different conditions. These characterizations were used to identify the onset of the corrosion

process in this work. The traditional 3-electrode CA approach was not suitable for accurate analysis of the solid-solid reaction, where oxidation and reduction reactions occur simultaneously at the high temperature. Therefore, a 2-electrode chronoamperometric setup was utilized (Papers I to IV) in this work. A bias voltage of 200 mV was used to provide sufficient cathodic protection to the counter electrode steel piece to avoid alteration of its surface during the measurement, thereby offsetting the reference level and ensuring that the source of the measured current mainly originated from corrosion processes on the working electrode. This CA measurement setup detects excess electrons being produced on the working electrode (sample piece) and records this electron flow (oxidation current) signal in order to give the net result of all processes occurring at the working electrode surface. Hence, from an electrochemical viewpoint, this method does not enable quantitative determination such as the identification of all reactions taking place at the metal surface or determination of the amount of material converted in the reactions. However, the relative magnitude of the current as a function of time allows identifying the reaction onset or reaction rate in the overall process. For this purpose, the CA results of the oxidation currents were normalized for the qualitative comparison of the oxidation process induced by different salts. In this work, all the CA measurements have repeated at least 3 times for every salt under both conditions. The oxidation currents varied to a certain extent since the contact area was not identical in every experiment. However, after the normalization process, highly reproducible results in terms of the magnitude and trend of oxidation current were observed.

3.3 Experimental procedures

3.3.1 Measurements under stagnant conditions

In Papers I-III, the CA measurements were performed in a furnace-housed glass-rig containing stainless steel wires to provide the contact between the electrodes and the potentiostat (Palm Instruments EM-Stat) (Figure 2). The experimental setup was placed in a cold furnace covered by a custom-made lid with a heat-resistant window, which allows visual control of proper contact between the rectangular sample piece and the cylindrical counter/reference electrode piece. Initially, the cylindrical piece was raised and separated from the salt pellet, while a thin glass

piece separated the salt pellet from the sample piece. The temperature of the furnace was increased to the target temperature and stabilized. Then, the glass piece was removed, and the cylindrical piece was put down to create a closed circuit for the CA measurements. A 200 mV potential difference was applied to the test pieces for 3 minutes (Paper I) and 120 minutes (Papers I – III). The CA measurements were performed at two temperatures: 450 °C as a reference temperature, and 535 °C as a typical temperature of a superheater surface in a biomass-fired boiler. The temperature within the furnace was monitored by an external thermal probe, which was in direct contact with the sample holder. All these measurements were carried out in stagnant air. The reaction quenching and sampling times were deducted from CA data, as the current signal reflects the changes in reaction type and rate at a given time. After the CA measurements, the furnace was cooled down to room temperature with pure nitrogen. After this, the sample piece was taken out, and the salt pellet was removed from the surface of the sample. Then, the sample was studied by SEM and XPS. In addition, samples without salt were treated under the same experimental conditions and used as references in the XPS and SEM studies.

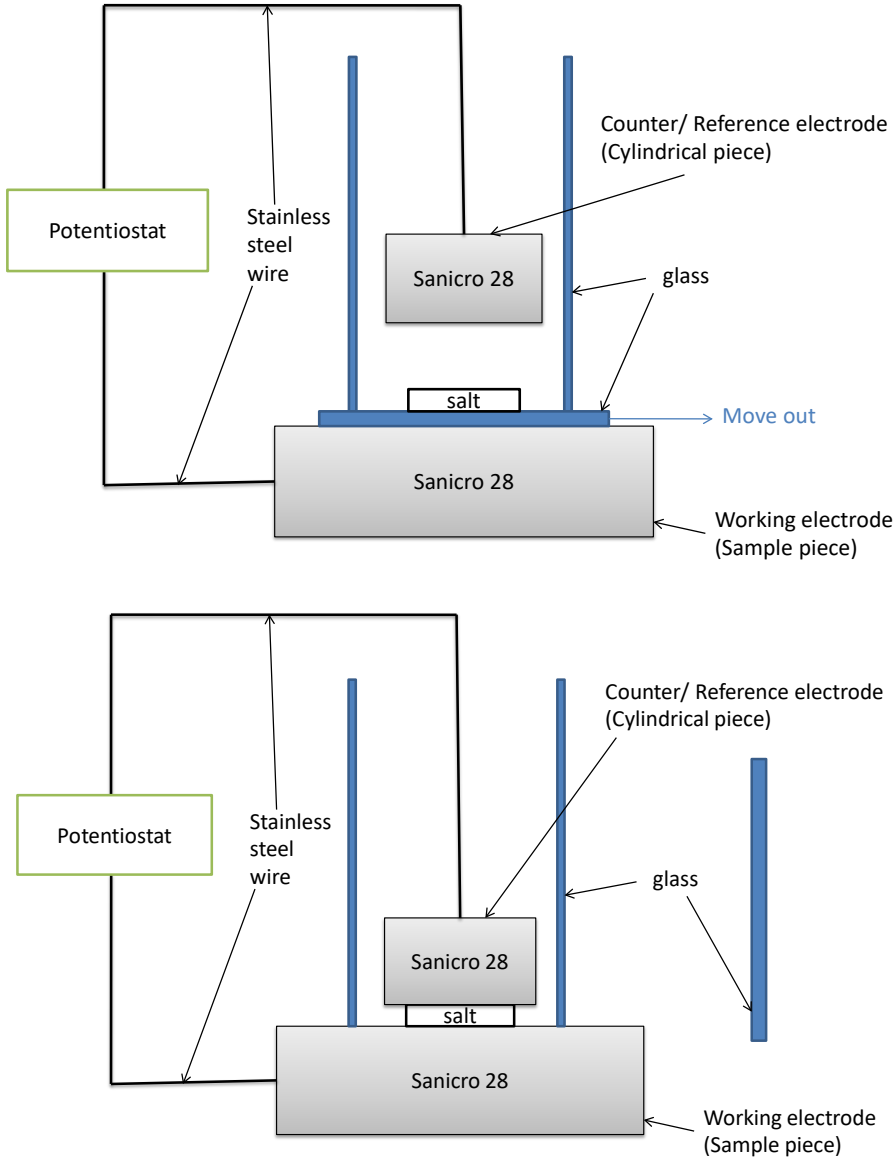

Figure 2. A schematic representation of the stagnant condition experimental setup. [Papers I, III]

3.3.2 Measurements under flowing conditions

In Paper IV, the exposures were conducted in a temperature-controlled horizontal tube furnace with a specially designed sample holder (Figure 3). The exposure temperature 535 °C was measured with a thermocouple installed at the end of the sample holder. The heating process was carried

out under flowing nitrogen with the flow rate of 1 L·min^{-1} for 120 min until the temperature was stable. After that, the CA measurements were continued at 535 °C for 120 min in two studied atmospheres: i) dry air, and ii) dry air with 30% H_2O introduced with a flow rate of 1 L·min^{-1}. After two hours, the gas flow was switched to nitrogen flow with 1 L·min^{-1} in order to stop possible oxidation reactions, and the furnace was cooled down to room temperature. The salt pellets were carefully removed from the cooled sample surfaces. The surface morphology of the samples was studied using SEM-EDX while the thickness and composition of the oxide layer were analyzed with XPS.

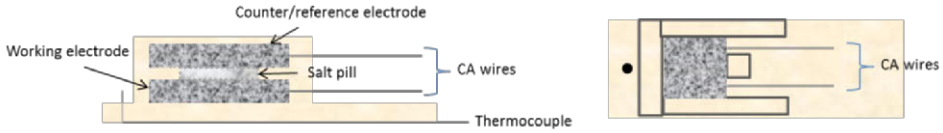

Figure 3. A schematic representation of the sample holder: side view (left) and top view (right). [Papers IV]

3.3.3 Measurements with different oxygen sources

In Paper V, the high-temperature exposures were conducted in a temperature-controlled tube furnace (Figure 4), where the samples were positioned horizontally and parallel to the gas flow direction inside a quartz reactor. The exposure temperature 540 °C was measured with thermocouples installed in the middle and at both ends of the sample holder. The heating was carried out in flowing nitrogen at a heating rate of 5 °C min^{-1} and the test atmosphere was introduced at the target temperature through a flow of 2 dm^{2}min^{-1} for 15 min, after which the reactor was sealed tightly. In these measurements, two different stagnant atmospheres were studied: i) synthetic air (20% $^{16}O_2$ and 80% N_2) and ii) synthetic air ($^{16}O_2$ and N_2) with over 30% isotope-enriched water $H_2{}^{18}O$ containing the ^{18}O isotope (^{18}O content>98%, GMP quality, Rotem Industries Ltd., Israel). In addition to these two atmospheres, as a reference, the samples exposed in the synthetic air in the absence of the KCl pellet were studied. With the furnace at the target temperature, the ^{18}O-enriched water was injected into the reactor, where it was immediately vaporized. Therefore, the created overpressure was vented out, making a determination of the exact humidity level difficult. However, the presence of labeled oxygen in the humidity and the

humidity levels are sufficient to provide qualitative information to the ToF-SIMS analysis.

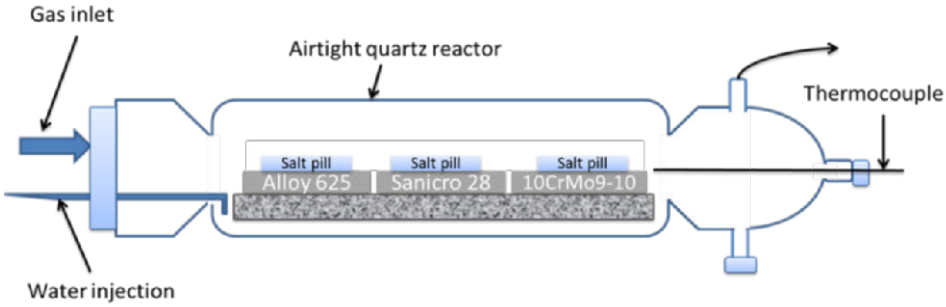

Figure 4. A schematic representation of the flowing condition experimental setup. [Paper V]

After each exposure, the furnace was cooled down to room temperature while purging the reactor with pure nitrogen to avoid the continuation of any potential oxygen-involving reaction. Then, the cylindrical salt pellets were removed from the sample surfaces. After the exposure, SEM-EDX was used for the surface morphology analysis, XPS was used for oxide thickness and composition analyses while ToF-SIMS was used to distinguish ^{16}O from ^{18}O. In this experiment, the presence of the two oxygen isotopes in the corrosion products gives information on the origin of oxygen, i.e. oxygen in the air ^{16}O, or oxygen in the water ^{18}O.

3.4 Methods for analyzing the produced reaction layer

3.4.1 X-ray photoelectron spectroscopy (XPS) measurements

After the exposures, the samples were analyzed using XPS. XPS provides quantitative and chemical state information from the surface of the studied material. XPS is accomplished by exciting the surface of a sample with mono-energetic Al kα X-rays which causes photoelectrons to be emitted from the sample surface. The energy of the emitted photoelectrons is determined by an electron energy analyzer. From the binding energy and photoelectron peak's intensity, the elemental identity, chemical state, and quantity of a detected element can be measured. Spatial distribution information can be obtained by scanning the micro-focused X-ray beam across the sample surface and depth distribution

information can be obtained by combining XPS measurements with sputtering to characterize thin film structures.

In this work, XPS measurements were carried out with a Physical Electronics Quantum 2000 Instrument combined with a monochromatic Al Kα X-ray excitation, operated at 22.8W, and charge compensation by using an electron filament and an electron gun. The analysis area was 1 x 1 mm^2, and the take-off angle was 45° to the sample surface. The sputtering was performed by using the pass energy of 117.40 eV for 6 min for each analysis point. Curve-fitting Multipak 9.5 software was used to analyze the oxide layer composition. XPS provided information of the elemental distribution on the metal surface. It also detected the individual chemical states of each element. XPS data were utilized to measure the chemical states of chromium and the ratio of hexavalent chromium (Cr^{6+}) to trivalent chromium (Cr^{3+}) to interpret the influence of salts on the alkali chromate formation. The ratio of Cr^{6+}/Cr^{3+} was used to reflect the amount of alkali chromate formed in the sample surface. In the Cr spectra, three separate peaks were observed at binding energies (BE) 579.20, 576.83, and 575.58 eV. The peaks at 576.83 and 575.58 eV were assigned to Cr^{3+}, most likely originating from Cr_2O_3, while the peak located at 579.20 eV was assigned to CrO_4^{2-} [78], indicating the presence of alkali chromate. Additionally, during the sputtering process, the oxide layer penetration time was measured. The oxide layer thickness was calculated from the layer penetration by using calibration data and standard equations[79].

It should be noticed that the XPS technique has limitations concerning surface sputtering. After the exposure, the sample surface was uneven as it was covered by some alkali chromate crystals of different sizes. Under these crystals, the surface was covered by a dense and thin oxide layer. The sputtering time of the thin oxide layer was shorter than that of the thicker alkali chromate crystals. Thus, the thin oxide layers were sputtered down to the bulk metal much faster than the thicker crystals. The depth profiles of the oxides were shown in the XPS graphs, where the resulting signal was both from the alkali chromate crystals and from the metal oxide between the crystals. Hence, the slow decrease of the oxygen concentration in the depth profiles made it difficult to interpret the exact thickness of the formed oxide. Therefore, the approximate reaction layer thickness was defined instead of an exact value for the

alkali chromate crystal thickness or the oxide layer thickness. The reaction layer was considered to be sputtered through when the oxygen atomic concentration had decreased to 50% of its initial concentration.

3.4.2 Scanning electron microscope (SEM) measurements

SEM is a frequently used technique to detect the surface morphology and to analyze the average composition of corroded surfaces. SEM is a type of electron microscope which uses a focused beam of electrons to provide a magnified image by scanning the sample. The electrons interact with atoms in the sample, producing various signals which contain information about the surface topography and composition of the sample. The electron beam is scanned in a raster scan pattern, and the position of the beam is combined with the intensity of the detected signal to produce an image. In this thesis, an SEM-EDX (SEM – LEO Gemini 1530 with a ThermoNORAN Vantage X-ray analyzing system manufactured by Thermo Scientific) was used in Papers I – III. The SEM was operated in the secondary electron mode at an accelerating voltage of 15 kV for imaging with an aperture size of 60μm. SEM micrographs were recorded with 30x to 10kx magnifications.

3.4.3 Time-of-flight secondary ion mass spectrometry (ToF-SIMS) measurements

ToF-SIMS provides elemental, chemical state, and molecular information from surfaces of solid materials. The surface of a sample is exited with a finely focused ion beam which causes secondary ions and ion clusters to be emitted from the surface of the sample. A time-of-flight analyzer is used to measure the exact mass of the emitted ions and clusters. The identity of an element or molecular fragments can be obtained from the exact mass and intensity of the SIMS peak. Spatial distribution information is obtained by scanning a micro-focused ion beam across the sample surface.

The samples exposed to the atmosphere containing the ^{18}O isotope were analyzed by means of Time-of-flight secondary ion mass spectrometry (ToF-SIMS) (PHI TRIFT II, ULVAC-PHI Inc.) to distinguish ^{16}O originality from the synthetic air and ^{18}O originality from the isotope labeled water. The measurements were carried out by using 25 kV Ga^+ ions and an analysis spot with a diameter of one micrometer and an

analysis depth of around five nanometers. The gallium ions sever atoms and/or atom groups from the sample surface, after which the severed species can be distinguished and identified by their masses.

4. Results and discussion

This section presented the visual observation of the salts induced sample surfaces and the CA results (Papers I–V) after the two-hour exposure. XPS results (Paper III and IV) for the exposure test of Sanicro 28 in the presence of the three alkali salts under stagnant and flowing conditions were summarized, and three comprehensive tables overviewed the elemental distribution results and the Cr^{6+}/Cr^{3+}-ratio results in XPS measurements. After these results, the corrosion effect of the three individual alkali salts was discussed based on the SEM images of exposed samples based on Papers I-V.

4.1 Visual observation

All the Sanicro 28 samples exposed to KCl, K_2CO_3 and NaCl at 450 °C and 535 °C (Paper I-V) had a similar visual appearance. The changes in the surface morphology of the steel surface after the two-hour exposure at the test temperature are schematically illustrated in Figure 5. The metal surface directly below the salt pellet showed the most severe attack and the ring-shaped area surrounding the pellet showed limited changes while the remaining surface showed only minor effects. The main difference between the samples exposed at 450 °C and 535 °C was that the edges of the salt-influenced area were clear at 535 °C.

In order to study the mechanisms of the salt-induced oxidation under stagnant conditions, three locations were selected from every sample exposed at 450 °C: the surface under the salt pellet with presumably low oxygen partial pressure (location a), the affected surface area just outside the salt pellet with higher oxygen partial pressure availability (location b), and the surface unaffected by the salts (location c), Figure 5A. Compared with the case at 450 °C, one more analysis location on the edge of the salt pellet was selected at 535 °C under stagnant conditions. At this temperature, four locations were analyzed from every sample: the sample surface under the salt pellet (location a); the sample surface on the edge of the salt pellet at high oxygen partial pressure (location b); the sample surface area around the salt pellet, where the surface was affected by salts based on visual observation (location c); and the surface unaffected by salts (location d), Figure 5B. Under flowing conditions, three locations were analyzed from every sample: the sample surface

under the salt pellet (location a in Figure 5B); the sample surface area around the salt pellet, where the surface was affected by salts based on visual observation (location c in Figure 5B); and the surface unaffected by salts (location d in Figure 5B).

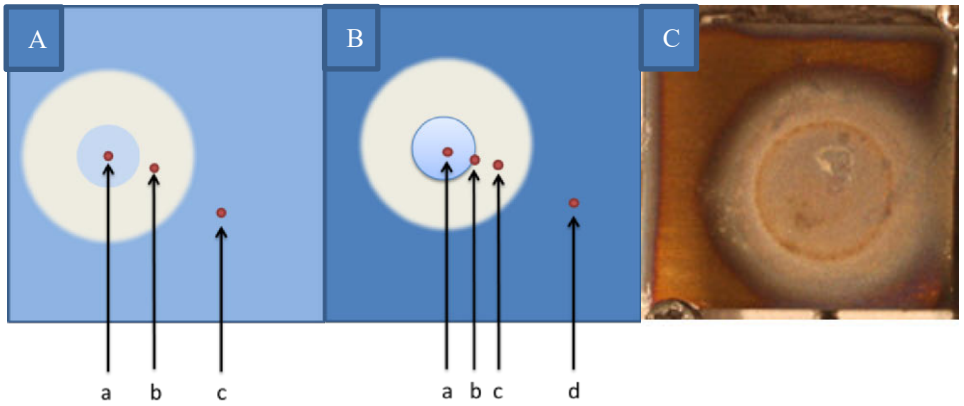

Figure 5. The analysis locations: A. 450 °C a) the sample surface under the salt pellet, b) the sample surface around the salt pellet, c) the unaffected surface; B. 535 °C. a) the sample surface under the salt pellet, b) the sample surface on the edge of the salt pellet, c) the sample surface around the salt pellet, d) the unaffected surface; C. One real sample surface image after exposure to K_2CO_3 at 535 °C. [Paper III, IV]

4.2 CA results

4.2.1 Corrosion current under stagnant conditions

Under stagnant conditions, highly reproducible results in terms of the magnitude and trend of oxidation current were obtained at 0 – 2 hours of the corrosion process in the presence of all three salts at 450 °C and 535 °C (Figure 6). There was some background noise coming from the intermittent heating of the furnace, causing the CA results to fluctuate but not affecting the overall trend. Measurements with K_2SO_4 under the same conditions were chosen as reference, because it has been reported to have only a minor effect on the corrosion rate and morphology of the corroded surface[54]. All the other studied salts exhibited relatively high oxidation current levels, which confirmed that the signals originated from the oxidation reactions rather than from the experimental setup. Comparing the overall current signals at 450 °C and 535 °C, the rates of

the oxidation reactions with all salts but K_2SO_4 were much higher at 535 °C, as expected.

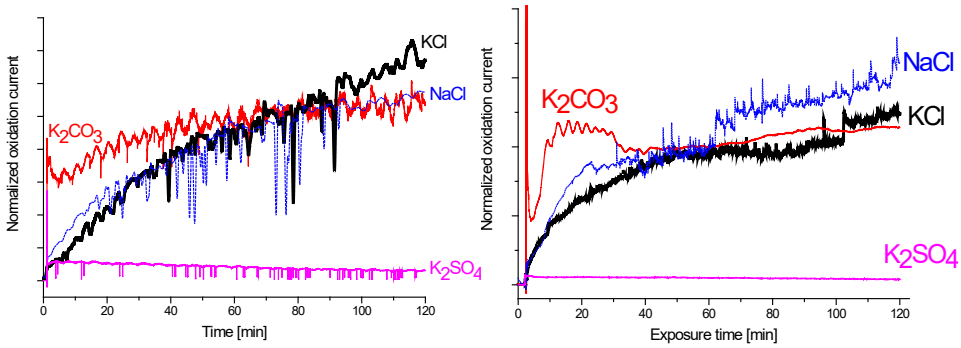

Figure 6. CA results for the oxidation reaction at 450 °C (left) and 535 °C (right) in the presence of KCl, NaCl, K_2CO_3 and K_2SO_4 (reference). The salt pellets were contacted with the sample at t = 1 minute. [Paper III]

In the presence of the chloride containing salts (KCl and NaCl), the measured currents displayed a similar trend at both temperatures, which indicated similar corrosion processes for these two salts. As shown in Figure 6, after the contact with the NaCl salt pellet (t = 1 min), the current signal grew slowly and gradually reached a steady state level (70 min at 450 °C and 50 min at 535 °C). At 450 °C, the current in the case of KCl seemed higher than that of NaCl at the steady state. This suggested that at least one or possibly several reactions occurred at a higher reaction rate in the presence of KCl. In contrast, at the higher temperature (535 °C), the current was higher in the case of NaCl than in the case of KCl. This indicated that at least one or possibly several reactions occurred with a higher reaction rate in the presence of NaCl at this temperature or that a new reaction pathway was activated.

When comparing the two potassium-containing salts (KCl and K_2CO_3), the measured currents showed different trends at both temperatures. At 450 °C, the oxidation current reached a high level immediately after contact in the case of K_2CO_3. After the initial reaction stage, the current gradually increased and reached a steady state at t = 40 min. The possible explanations could be the oxidation reaction or reactions were activated earlier for K_2CO_3 than for KCl, different ion mobilities, salt decomposition or even different reaction pathways for KCl and K_2CO_3. At 535 °C, the onset of the oxidation current was observed already at t =

12 min in the presence of K_2CO_3, and after this, the current decreased and reached a steady state at a similar level as with KCl at t = 38 min. This suggested that an oxidation reaction or a set of oxidation reactions were activated and progressing more easily in the presence of K_2CO_3. However, after the initial conversion stage, the net oxidation rate was decreased, which might be explained by a decreased rate of the oxidation reaction or a simultaneous occurrence of some reduction reactions.

4.2.2 Corrosion current under flowing conditions

Similar to the CA results under stagnant conditions, highly reproducible results in terms of the magnitude and the trend of the current were also obtained under flowing conditions in dry and the humid air (Figures 7 and 8). Under dry conditions, the CA currents were quite stable from room temperature (t = 0 h) to around 400 °C (t = 0.5 h). After that, the oxidation current of the samples exposed to KCl and K_2CO_3 started to increase. The oxidation current of the sample exposed to NaCl started to increase at a slightly higher temperature, 450 °C at t = 0.55 h. In contrast, the oxidation current of the sample exposed to K_2SO_4 started to increase when the temperature had reached 500 °C at t = 1 h. Based on the changes in the current signals during the two first hours in nitrogen, i.e. before the introduction of air, residues of oxygen in the furnace were assumed to induce oxidation of the material. The temperature difference for the oxidation current trends between the salts suggested that the reactions of the metal with KCl and K_2CO_3 started at lower temperatures than the reactions with NaCl. In addition, all these three salts reacted with the metal surface at much lower temperatures than K_2SO_4.

After the temperature had stabilized at 535 °C (t = 2 h), dry air was introduced into the furnace. Compared to the case with K_2SO_4, all the other studied salts (KCl, K_2CO_3, and NaCl) exhibited relatively high oxidation current levels and thus high oxidation rates. In the presence of the KCl and NaCl, the similar slow increase of the current signals suggested oxidation of the metal after the air introduction at t = 2 h. The current signal caused by KCl reached a steady state level at around t = 2.7 h, while for NaCl the current signal steadily increased during the exposure at 535 °C. Again, when comparing KCl and K_2CO_3, different shapes and magnitudes in the CA current curves were obtained. After the dry air was introduced (t = 2 h), K_2CO_3 initiated a much higher

oxidation current signal than KCl. However, after the initial conversion stage, the CA current signal level for K_2CO_3 steadily decreased.

In general, the currents under humid conditions were relatively noisy compared to those under dry conditions (Figure 8). However, the trends of the current under humid conditions could still be clearly identified and correlated with possible redox-reactions taking place between the salts and the steel.

Compared with dry conditions, the most distinct differences in the normalized current signals at humid conditions were observed in the presence of NaCl and K_2CO_3. For NaCl, the current signal first stayed relatively steady for a short time after the humidity and air were introduced at t > 2h. If there were some initial reactions with the humid air, they did not contribute to the net oxidation current signals. At about t = 2.6 h, the current signal started to stepwise increase, due to one or possibly several oxidation reactions. For K_2CO_3, the current signal under humid conditions did not show a similar fast initial oxidation reaction as under dry conditions. The CA current signal and thus the oxidation reaction rate was significantly lower and of the same level as the current signals measured for the steels exposed to KCl and NaCl.

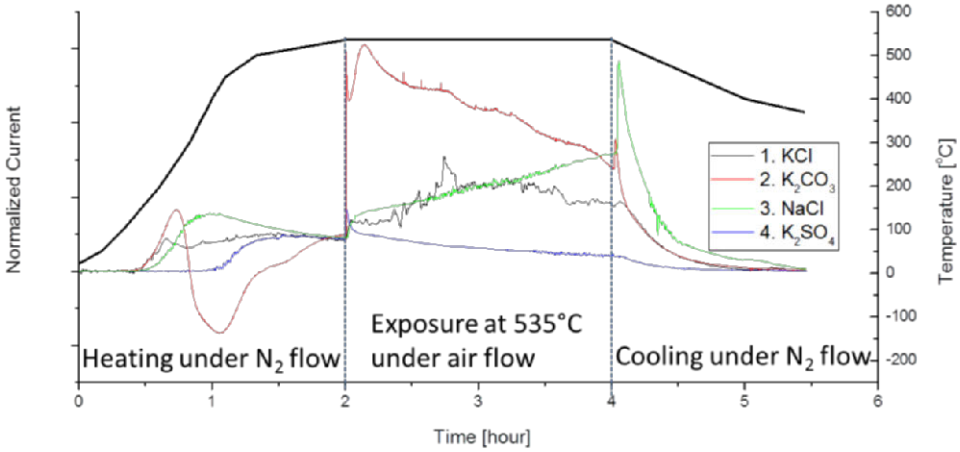

Figure 7. Normalized CA results for the oxidation reactions at 535 °C in the presence of KCl, NaCl, K_2CO_3 and K_2SO_4. The system was filled with nitrogen when it was heated up. At t = 2 h the dry air was introduced into the system with a flow rate of 1 $L \cdot min^{-1}$ and at t = 4 h the heating was terminated, air flow was closed and nitrogen introduced.

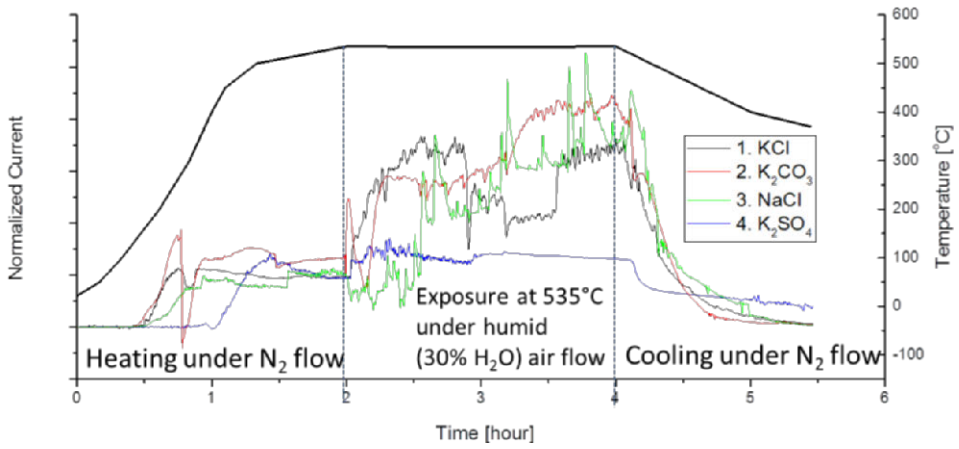

Figure 8. Normalized CA results for the oxidation reactions at 535 °C in the presence of KCl, NaCl, K_2CO_3 and K_2SO_4. The system was filled with nitrogen when it was heated up. At t = 2 h the air with 30% moisture was introduced into the system with a flow rate of 1 L·min^{-1} and at t = 4 h the heating was terminated, air flow was closed and nitrogen introduced.

4.3 XPS results

All the samples were analyzed with XPS after the CA measurements (Papers I–IV). In the XPS measurements, the surface of the sample was analyzed using an elemental spectra process and a depth profile sputtering process. The depth profile gave the chemical composition and the approximate reaction layer thickness, whereas the spectra of Cr electron core levels showed the elemental composition of the sample surface. Figure 9a shows the depth profile for the elements in the area under the salt pellet (location a in Figure 5B) for the sample exposed to KCl at 535 °C in stagnant air. The approximate thickness of the reaction layer is given with the dashed line. The spectra of Cr electron core level and the composition in the same location (location a in Figure 5B) is shown in Figure 9b. The Cr^{6+}/Cr^{3+}-ratio could be obtained by calculating the ratios of corresponding peak areas.

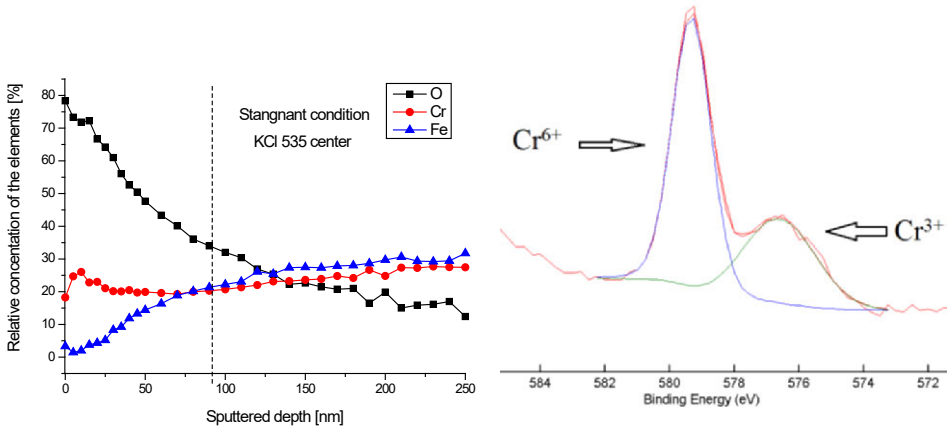

Figure 9. Relative atomic concentrations in the steel surface exposed to KCl at 535 °C in stagnant air. The analysis is for the area under the salt pellet (location a in Figure 5B). b) Chromium profile of the oxide layer after 120min at 535 °C.

In order to compare the XPS results, the approximate reaction layer thicknesses based on the XPS depth profile at each location (locations a-c in Figure 5A) are summarized in Table 2 (Paper III). Table 3 summarizes the relative Cr^{6+}/Cr^{3+} ratio at the same locations of the sample from spectra of Cr electron core level results (Paper III). Table 4 summarizes the approximate reaction layer thickness based on the XPS depth profile at each location (Paper IV).

Table 2. The approximate reaction layer thickness (nm) at locations a-c in Figure 5A and a-d in Figure 5B after 2-hour exposure to KCl, NaCl and K_2CO_3 at 450 °C and 535 °C under stagnant conditions. The values are based on the reaction layer thickness derived from the XPS depth profile (Paper III).

The approximate reaction layer thickness (nm)								
	450°C				535°C			
	Under the salt pill	Around the salt pill	The unaffected surface		Under the salt pill	On the edge of the salt pill	Around the salt pill	The unaffected surface
	A	B	C		A	B	C	D
No salt	N.A.	N.A.	17		N.A.	N.A.	N.A.	48
KCl	22	22	17		90	135	140	48
K2CO3	22	23	18		115	115	118	48
NaCl	22	23	17		70	85	80	47

Table 3. The relative Cr^{6+}/Cr^{3+} ratio at locations a-c in Figure 5A and a-d in Figure 5B after two hours of exposure to KCl, NaCl and K_2CO_3 at 450 °C and 535 °C under stagnant conditions. The values are calculated based on Cr^{6+}/Cr^{3+} ratio from the spectra of Cr electron core level results (Paper III).

The relative Cr6+/Cr3+ ratio								
	450°C				535°C			
	Under the salt pill	Around the salt pill	The unaffected surface		Under the salt pill	On the edge of the salt pill	Around the salt pill	The unaffected surface
	A	B	C		A	B	C	D
No salt	N.A.	N.A.	no Cr6+		N.A.	N.A.	N.A.	no Cr6+
KCl	9:1	2:3	3:7		3:2	4:1	3:7	1:9
K2CO3	9:1	3:7	1:4		1:1	3:2	1:4	1:9
NaCl	7:3	2:3	3:7		3:7	1:4	1:9	1:9

Table 4. The approximate reaction layer thickness (nm) at locations a,c and d in Figure 5B after two hours of exposure to K_2SO_4, KCl, NaCl and K_2CO_3 at 535 °C under flowing conditions. The values are based on the reaction layer thickness derived from the XPS depth profile (Paper IV).

The approximate reaction layer thickness (nm)							
	Under dry conditions				Under wet conditions		
	Under the salt pill	Around the salt pill	The unaffected surface		Under the salt pill	Around the salt pill	The unaffected surface
	A	C	D		A	C	D
K2SO4	90	N.A.	90		110	N.A.	110
KCl	95	100	80		120	400	110
K2CO3	300	90	90		500	160	120
NaCl	200	220	130		200	120	180

4.4 Potassium chloride induced corrosion

4.4.1 Dry conditions

This section discusses the results of KCl-induced corrosion of Sanicro 28 samples at 450 °C and 535 °C under dry condition (Papers I-V). The XPS results indicated that the reaction layer thickness at the steel sample increased when exposed to KCl and with increasing the temperature. Figures 10 and 11 present the morphologies of the sample surfaces after the exposure to KCl for 2 hours at 450 °C and 535 ºC. In the contact area with the salt pellet (Fig. 10a and Fig. 11a, b), potassium chromate crystals were identified on the surfaces. Data obtained using SEM correlated with XPS-results, which suggested a high ratio of Cr^{6+}/Cr^{3+} in the area under the pellet. This verified that KCl reacted with the protective oxide layer and formed potassium chromate crystals on Sanicro 28 steel sample. Further, the potassium chromate crystals were much larger on the sample exposed to 535 °C than at 450 °C. The potassium chromate crystal formation was proposed to progress as follows: firstly, KCl reacts with the protective chromium oxide forming small chromate crystals on the oxide layer; as the chromate crystal formation continues, the small crystals coalesce into larger ones at a higher temperature (535 °C). These visible large chromate crystals increase the overall reaction layer thickness.

The elemental distribution of the chromium-rich oxide layer was homogeneous in the sample exposed to 450 °C. In contrast, an iron-rich inner layer and a chromium-rich outer layer formed under the salt pellet and around the salt pellet in the sample exposed to 535 °C (Paper III). This observation correlated with the lower Cr^{6+}/Cr^{3+} -ratio was given by the XPS measurements of the sample exposed to 535 °C. Thus, the conversion of the initial chromium oxide to potassium chromate was dominant at 450 °C. At 535 °C, the initial thin chromium oxide reacted with KCl, forming potassium chromate crystals on the surface. Simultaneously, chloride ions diffused to the metal/oxide interface and reacted with the bulk steel to form metal chlorides. Then, the volatile metal chlorides diffused back to the surface via the voids in the oxide layer to react with oxygen, forming metal oxides on the surface under the potassium chromate crystals[14,31].

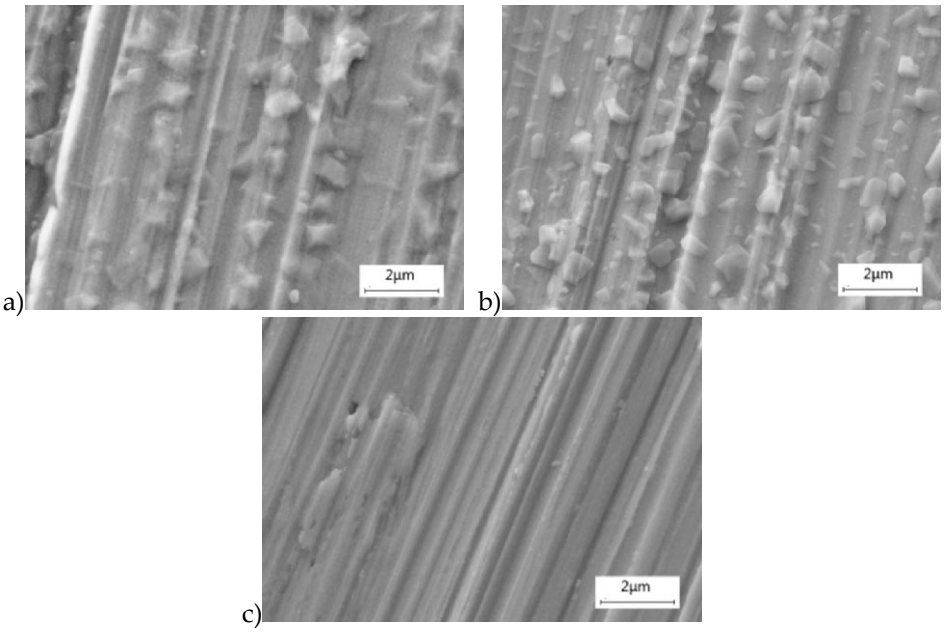

Figure 10. Secondary electron images of Sanicro 28 surfaces exposed to KCl at 450 °C for 120 min under dry stagnant conditions. The images were taken from a) the surface under the salt pellet (location a in Fig. 5A); b) the affected surface around the salt pellet (location t b in Fig. 5A); c) the unaffected surface (location c in Fig. 5A). [Paper III]

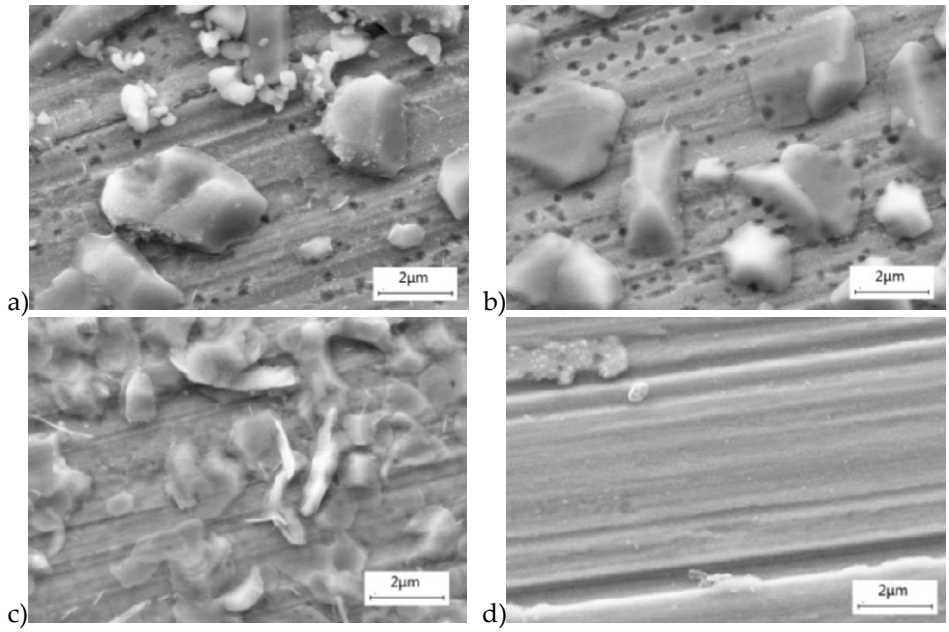

Figure 11. Secondary electron images of Sanicro 28 surfaces exposed to KCl at 535 °C for 120 min under dry stagnant conditions. The images were taken from a) the surface under the salt pellet (location a in Fig. 5B), b) the surface on the edge of the salt pellet (location b in Fig. 5B), c) the affected surface around the salt pellet (location c in Fig. 5B), d) the unaffected surface (location d in Fig. 5B). [Paper III]

In the area outside the salt pellet (Fig. 10b and Fig. 11c), a relatively thick oxide layer and high amounts of Cr^{6+} were detected, which suggested that KCl diffuses via gas phase and along the surface to promote potassium chromate formation. Compared to the area in direct contact with the salt pellet, the potassium chromate crystals were less in number and smaller in size while the chromium- and iron-containing oxide was thicker. The reason was that the area outside the salt pellet had a higher availability of oxygen, and thus the chromium and iron had higher oxidation reaction rates to form metal oxides.

When comparing the unaffected area of the sample exposed to KCl (Fig. 10c and Fig. 11d) with the blank sample, the elemental distributions and the reaction layer thickness were identical. The depth profiles showed chromium and oxygen-rich signals, indicating the formation of a thin protective chromium oxide layer on the surface at 450 °C. At 535 °C, a much thicker reaction layer was observed in the same locations (Fig. 11d).

Thus, a thicker protective chromium oxide formed on the sample surfaces at the higher temperature.

Under dry flowing gas conditions (Paper IV), several small nodules of K_2CrO_4 crystals together with tiny needles were identified on an uneven/porous oxide layer beneath the salt pellet (Figure 12a). In contrast, in the narrow ring-shaped area of the steel surface around the salt pellet, similar but fewer and smaller K_2CrO_4 crystals formations could be seen (Figure 12b). No clear indications of alkali chromate crystals but some very small needlelike crystals were seen on the sample surface further away from the area exposed to the salt pellets (Figure 12c). The surface morphology was similar to that observed in the stagnant conditions. However, the size and amount of the K_2CrO_4 crystals were much less and smaller than under stagnant conditions.

It was assumed that the gas flow in the experimental setup might have diluted the concentration of the evaporated gaseous alkali chlorides or even flushed them away. This would affect the gas phase diffusion of any evaporated salt to the steel surfaces not in direct contact with the salt pellet (locations c, d in Figure 5B). In this work, the metal surfaces around the salt pellets were affected (Figures 12b), thus suggesting that KCl diffused from the pellet along the metal surface. Compared to the results under stagnant conditions, the surface alteration indicated that KCl diffuses both through the gas phase and the surface.

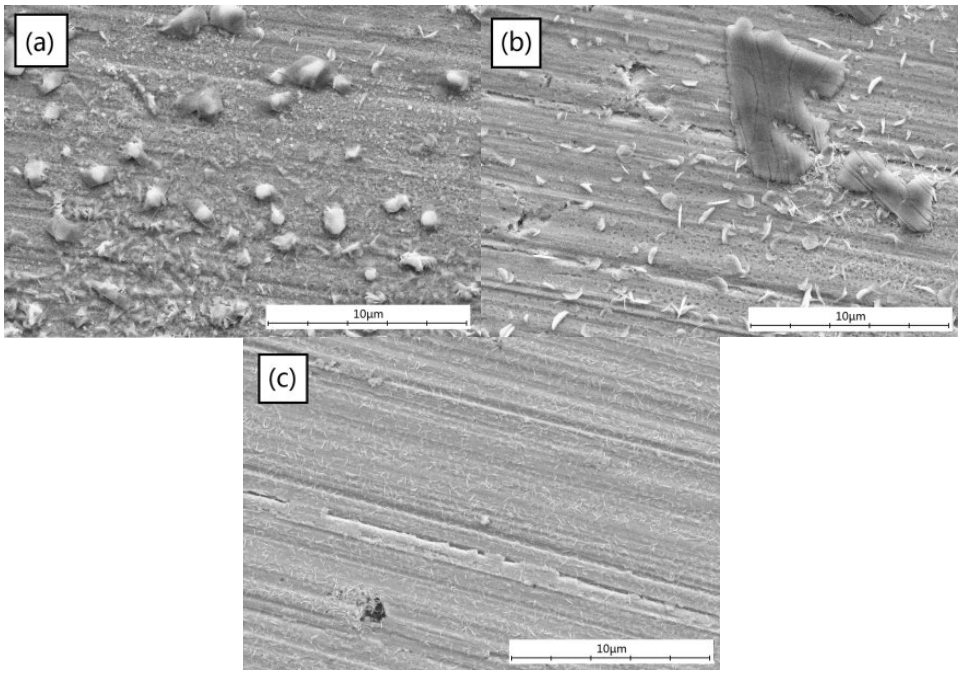

Figure 12. Secondary electron images of Sanicro 28 surfaces exposed to KCl at 535 °C for 120 min under dry flowing conditions. The images were taken from a) the surface under the salt pellet (location a in Figure 5B), b) the surface around the salt pellet (location c in Figure 5B) and c) the surface far from the salt pellet (location d in Figure 5B). [Paper IV]

4.4.2 Humid conditions

The morphology of the sample surface exposed to KCl under humid conditions (Figure 13) was different to that formed under dry conditions (Figure 12). A markedly larger amount of K_2CrO_4 crystals were formed beneath the salt pellet (Figure 13a) and at the edge of the salt pellet (Figure 13b). This result is in accordance with the previous results suggesting that a greater thermodynamic driving force leads to a more rapid formation of K_2CrO_4 in the humid environment[46]. Under humid conditions, thermodynamically stable HCl might form during the initial stage, which in turn contributes to the synergistic corrosion accelerated by the effect of water vapor[31]. Thus, the initial reaction could be correlated to Eq. 17. After this initial reaction, not only the chloride anions but also the formed HCl were able to diffuse into the bulk material and chlorinate the alloying metal inside, forming volatile metal chlorides. The driving force of the chloride species to diffuse inwards

was caused by the concentration gradient[51]. The metal chlorides might diffuse back to the metal surface and react with oxygen and water vapor, yielding a porous oxide and releasing the HCl that reinitiates the chlorination reaction[14].

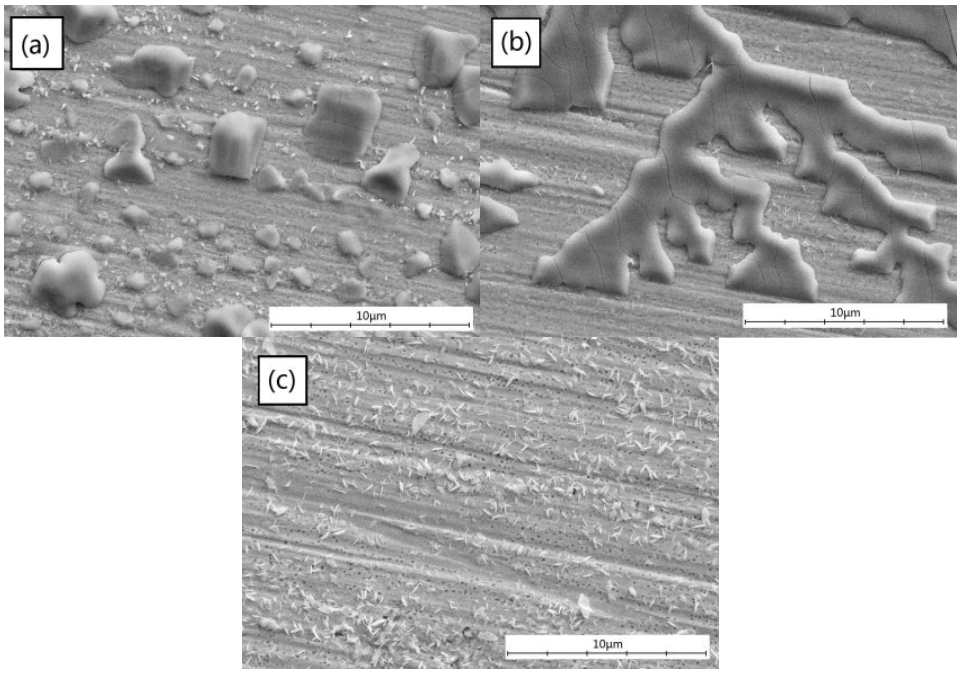

Figure 13. Secondary electron images of Sanicro 28 surfaces exposed for 120 min at 535 °C to KCl under humid flowing conditions. The images were taken from a) the surface under the salt pellet (location a in Figure 5B), b) the surface around the salt pellet (location c in Figure 5B) and c) the surface far from the salt pellet (location d in Figure 5B). [Paper IV]

4.4.3 The role of different oxygen sources on the corrosion mechanism

Since the role of humidity on the KCl-induced corrosion process was elusive, water labeled with the stable isotope of oxygen (^{18}O), $H_2{}^{18}O$, was utilized to track the detailed reaction mechanisms involved in the oxidation/corrosion process (Paper V). ToF-SIMS was utilized to distinguish the two oxygen isotopes ^{16}O and ^{18}O in the oxide layer at the metal surface. Since ^{16}O originates mainly from the molecular oxygen and ^{18}O originates from the water molecule, the impact on the oxygen origin on the corrosion reactions can be studied. According to the ToF-SIMS results shown in Figure 14, the particles on the surface consisted of potassium, chromium, and oxygen, i.e. K_2CrO_4 crystals. The two oxygen

isotopes could be identified clearly. It appeared that the formed K_2CrO_4 crystals contained a higher amount of ^{16}O from the air (65%) than ^{18}O from the water molecules (35%). In contrast, the chromium-rich oxide layer on the sample surface contained almost equal amounts of ^{16}O (52%) and ^{18}O (48%). These observations were explained as follows: during the pre-treatment, a protective chromium oxide layer containing ^{16}O isotope atoms formed and covered the sample surface. This chromium oxide was involved in the initial corrosion reaction with KCl, resulting in K_2CrO_4 crystals rich in ^{16}O isotope atoms. Water vapor was most likely adsorbed to the sample surface and involved in the oxidation reactions with iron and chromium, as also reported by Lu and Hultquist[80]. The analyzed ^{18}O-to-^{16}O isotope ratio in the formed surface oxide was higher than the calculated element ratio based on the adsorption of water molecules in the oxide. This illustrated that water vapor has a higher reaction rate than the oxygen molecules. In addition, the presence of ^{18}O in the chromate crystals indicated that the humidity also played a role in the chromate formation.

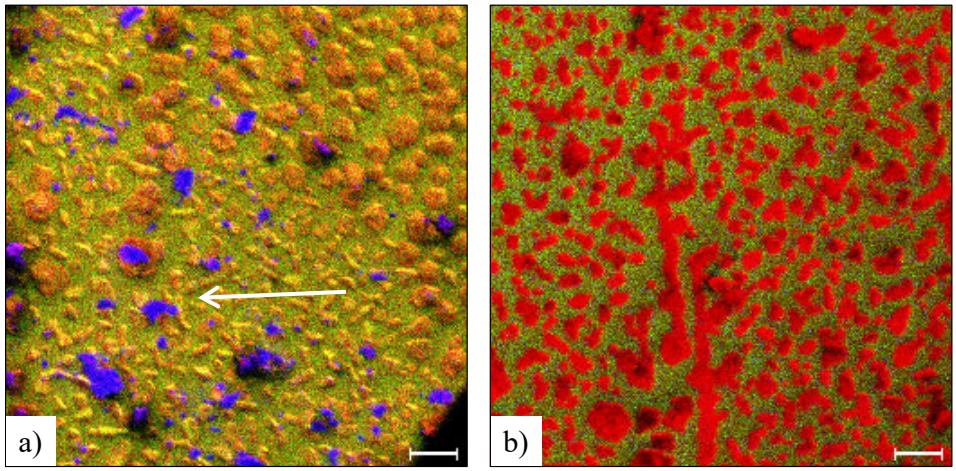

Figure 14. ToF-SIMS images of Sanicro 28 steel surface exposed to KCl at 540 °C for 120 minutes in synthetic air with $H_2{}^{18}O$; a) ^{16}O is red, ^{18}O is green, and Cl is blue, b) Fe is green and K is red. The scale bar equals 10 μm. The arrows in the images show the same reference point. [Paper V]

4.5 Sodium chloride induced corrosion

4.5.1 Dry conditions

In this section, the tests of Sanicro 28 samples exposed to NaCl for 2 hours at 450 °C and 535 °C under dry condition (Papers II-IV) are discussed. In general, the oxide layer thickness of the NaCl exposed steel samples had a thicker oxide layer than samples not exposed to the salt, and the layer thickness increased with temperature. Figures 15 and 16 present the NaCl-induced surface morphologies of the sample surface under stagnant conditions (Paper III). Figure 17 presents the NaCl-induced surface morphologies of the samples under flowing conditions (Paper IV). NaCl-exposed sample surface has a similar overall elemental distribution and surface morphology as KCl-exposed sample both under stagnant conditions and under dry flowing conditions. Alkali chromate crystals are also present on the salt-affected area (Figs. 15a, b, Figs. 16a–c and Figs. 17a, b) at both temperatures. The area far from the salt pellet (Fig. 15c, Fig. 16d and Fig. 17c) is identical with the blank sample.

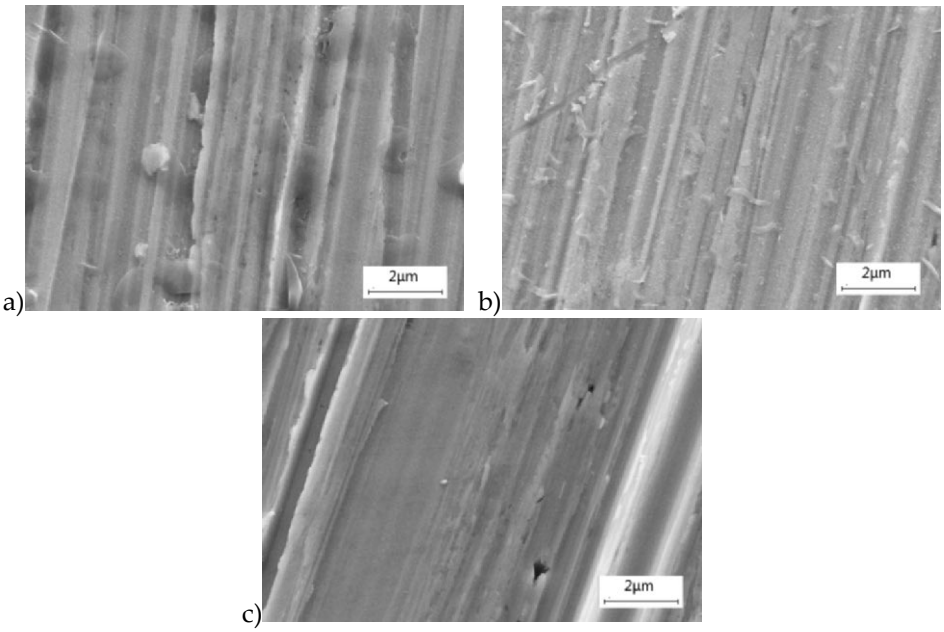

Figure 15. Secondary electron images of Sanicro 28 surfaces exposed to NaCl at 450 °C for 120 min under dry stagnant conditions. The images were taken from a) the surface under the salt pellet (location a in Fig. 5A); b) the affected surface around the salt pellet (location b in Fig. 5A); c) the unaffected surface (location c in Fig. 5A) [Paper III]

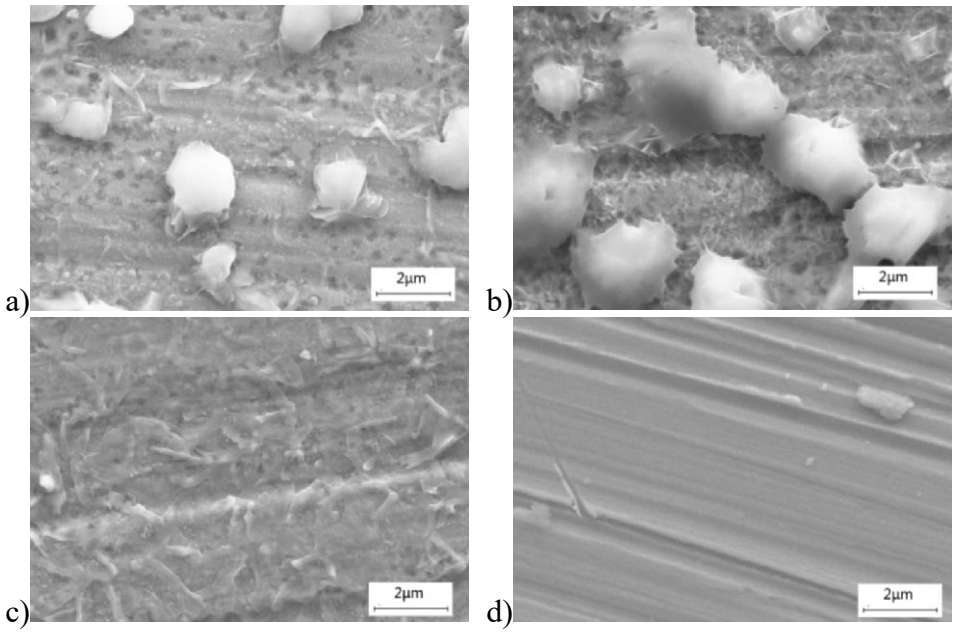

Figure 16. Secondary electron images of Sanicro 28 surfaces exposed to NaCl at 535 °C for 120 min under dry stagnant conditions. The images were taken from a) the surface under the salt pellet (location a in Fig. 5B), b) the surface on the edge of the salt pellet (location b in Fig. 5B), c) the affected surface around the salt pellet (location c in Fig. 5B), d) the unaffected surface (location d in Fig. 5B). [Paper III]

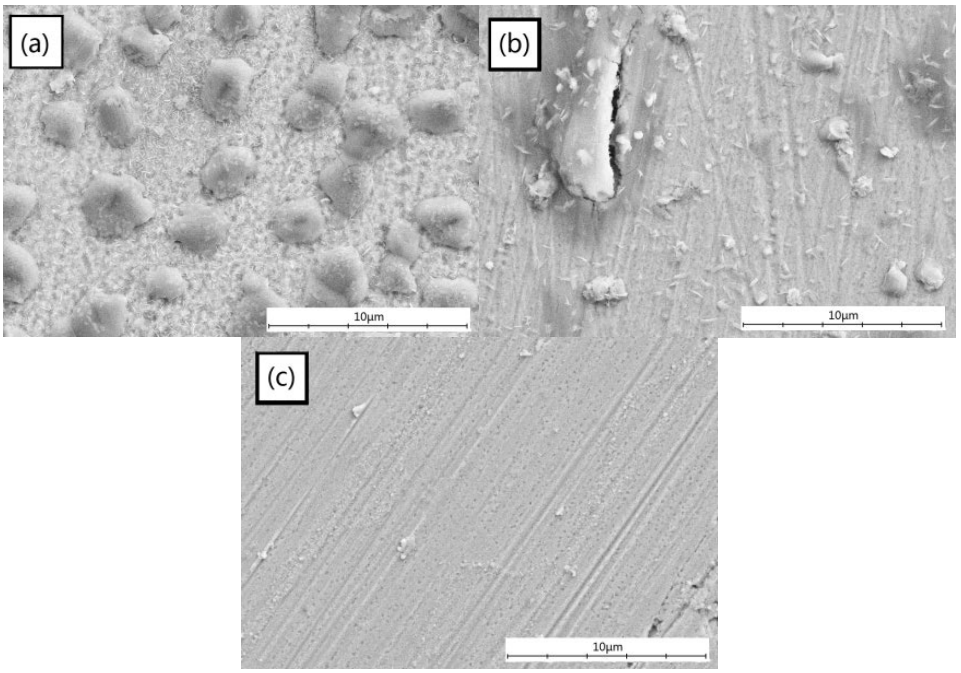

Figure 17. Secondary electron images of Sanicro 28 surfaces exposed to NaCl at 535 °C for 120 min under dry flowing conditions. The images were taken from a) the surface under the salt pellet (location a in Figure 5B), b) the surface around the salt pellet (location c in Figure 5B) and c) the surface far from the salt pellet (location d in Figure 5B). [Papers IV]

Based on the similar surface morphologies of the samples and the relatively high Cr^{6+}/Cr^{3+} -ratio, NaCl had a similarly corrosive effect as KCl. Both alkali chlorides led to the formation of alkali chromate and oxidation of chromium and iron in the bulk material at 535 °C. Under stagnant conditions, the amount and the size of the alkali chromate crystals on the NaCl-exposed steel were slightly smaller compared with the KCl-exposed sample. However, the amounts of formed chromium and iron oxides were higher in the presence of NaCl than KCl. The reason for the lower chromate formation rate for NaCl was assumed due to the lower reactivity of the sodium ion in the initial protective layer breakdown process. Besides the sodium chromate formation, a substantial amount of iron and chromium (III) oxide formed earlier at a significantly faster rate. The observed higher oxidation current at the steady state in the CA measurements (Figure 6) supports this finding.

Under flowing conditions, larger Na_2CrO_4 nodules together with a network of tiny crystals were identified in the area beneath the salt pellet (Figure 17a) compared to the sample exposed to KCl. In the ring-shaped area around the salt pellet exposed surface (Figure 17b), the Na_2CrO_4 crystals were smaller than the K_2CrO_4 crystals. Since the exposure was run under flowing conditions, the gaseous species were assumed be affected by the gas flow. Thus, the results indicated that NaCl has a higher diffusion rate along the surface than KCl, as was also suggested by the relative high CA current signal in the presence of NaCl (Figure 7).

4.5.2 Humid conditions

The morphology of the sample surface exposed NaCl under humid conditions was different to that under dry conditions (Figures 17 and 18). Under humid conditions, the size of the alkali chromate crystals observed beneath the salt pellet was much smaller and no Na_2CrO_4 crystals were seen at the edge of the salt pellet (Figure 18b). However, the overall thickness of the chromium-rich oxide was higher. Similar to the sample exposed to KCl, NaCl has been reported to be involved in the alkali chromate formation under humid conditions[22]. NaCl was preferably reacted with iron oxide in the presence of water vapor and formed sodium ferrate (III) ($Na_2Fe_2O_4$) and hydrogen chloride (Eq. 22), whereas the reaction of KCl with iron oxide to potassium ferrate (Eq. 23) was kinetically hindered[22]. As a consequence, the formed hydrogen chloride reacted with the chromium and iron in the interface between scale and bulk material to form chromium and iron chlorides, which reacted further to chromium and iron oxides when sufficient amount of oxygen was available. The formation of $Na_2Fe_2O_4$ did not contribute the oxidation or reduction currents, as there were no changes in the oxidation state of the elements (Eq. 22). This suggests that in this work, the relatively low and steady CA current signal (Figure 8) was related to similar reactions taking place in the initial stage of the NaCl induced corrosion.

$$\mathbf{2NaCl(s) + Fe_2O_3(s) + H_2O(g) \rightarrow Na_2Fe_2O_4(s) + 2HCl(g)} \quad \textbf{(22)}$$

$$\mathbf{2KCl(s) + Fe_2O_3(s) + H_2O(g) \rightarrow K_2Fe_2O_4(s) + 2HCl(g)} \quad \textbf{(23)}$$

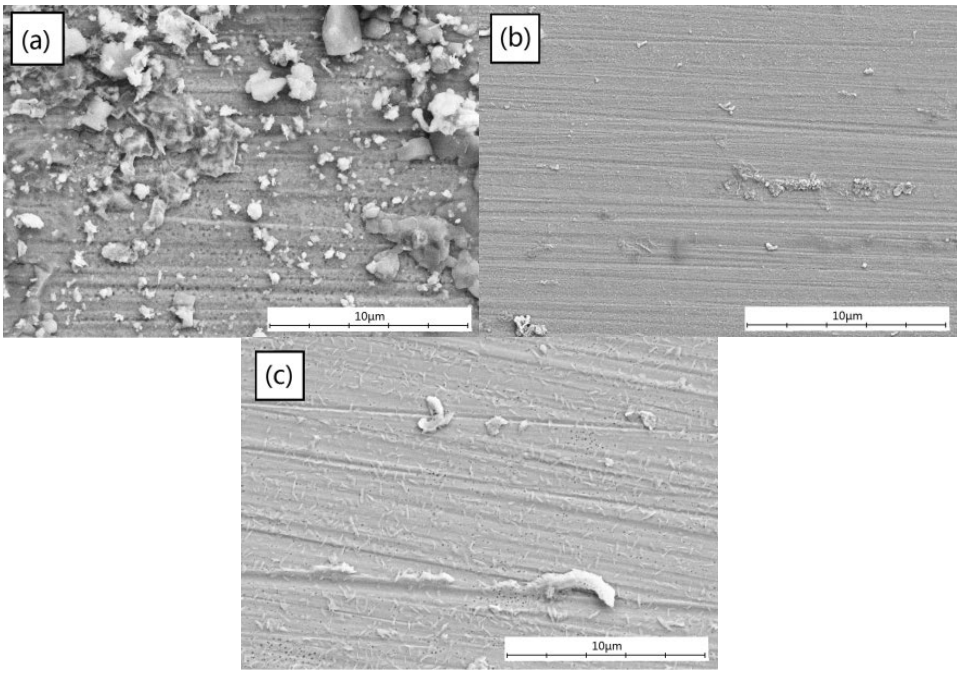

Figure 18. Secondary electron images of Sanicro 28 surfaces exposed for 120 min at 535 °C to NaCl under humid flowing conditions. The images were taken from a) the surface under the salt pellet (location a in Figure 5B), b) the surface around the salt pellet (location c in Figure 5B) and c) the surface far from the salt pellet (location d in Figure 5B). [Paper IV]

4.6 Potassium carbonate induced corrosion

4.6.1 Dry conditions

In this section, the results of Sanicro 28 samples exposed to K_2CO_3 for 2 hours at 450 °C and 535 °C under dry condition are discussed (Papers II-IV). In general, there was a clear oxide layer thickness growth and relatively high Cr^{6+}/Cr^{3+}-ratio at the areas influenced by K_2CO_3 both under stagnant and flowing conditions. This indicated that not only the alkali chlorides but also K_2CO_3 can react with the protective passivation layer to form potassium chromate crystals and thus contribute to the increase of the oxide layer thickness.

Figure 19 illustrates the surface morphology of Sanicro 28 after exposer to K_2CO_3 at 450 °C. The potassium chromate crystals on the surface under the salt pellet were needle-like (Fig. 19a), and the number of the crystals became less and their size smaller when moving out to the affected area

around the salt pellet (Fig. 19b). This indicated that K_2CO_3 initiated the potassium chromate formation when in direct contact with the steel, but the diffusion rate of K_2CO_3 via the gas phase and along the surface was much lower than that of KCl. The lower diffusivity of K_2CO_3 could be due to the lower vapor pressure compared to KCl.

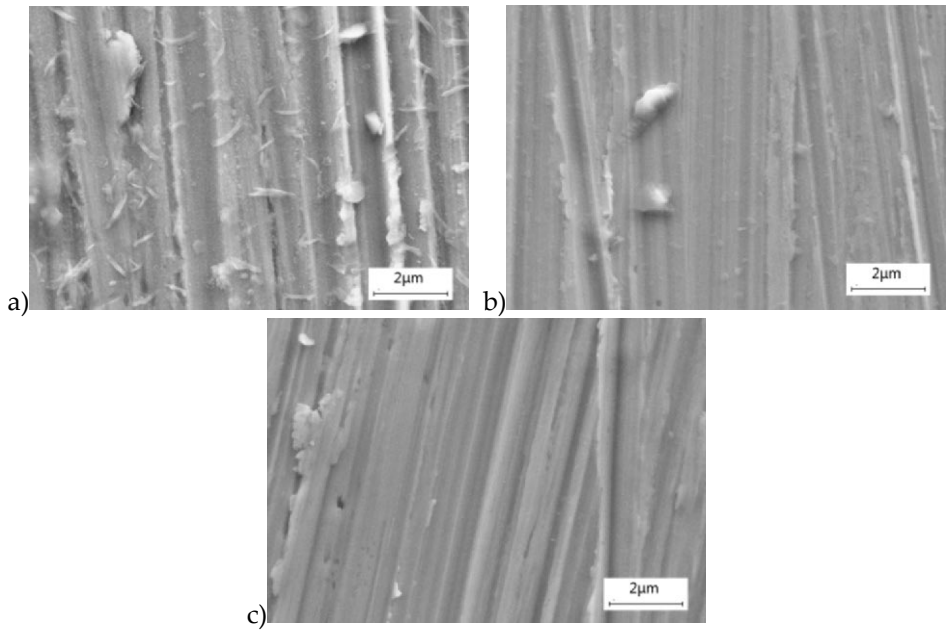

Figure 19. Secondary electron images of Sanicro 28 surfaces exposed to K_2CO_3 at 450 °C for 120 min under dry stagnant conditions. The images were taken from a) the surface under the salt pellet (location a in Fig. 5A); b) the affected surface around the salt pellet (location b in Fig. 5A); c) the unaffected surface (location c in Fig. 5A). [Paper III]

At 535 °C, larger chromate crystals formed on the surface under and the edge of the K_2CO_3 pellet (Fig. 20 a and b) in stagnant conditions. Also, the XPS results indicated a substantial increase in the reaction layer thicknesses after the exposure to the two potassium salts (KCl and K_2CO_3). In addition, under dry flowing conditions, numerous large K_2CrO_4 crystals were observed on the sample surface under the salt pellet (Figure 21a). Thus, K_2CrO_4 formed also in the absence of the chloride anion. Based on the SEM, XPS and CA results, the following reactions could be proposed at the metal surface in the presence of K_2CO_3. Fast initial and ongoing oxidation reactions occurred in the presence of K_2CO_3. These reactions were most likely induced by the presence of

potassium ions and attributed to the higher content of Cr^{6+}. Thus, K_2CrO_4 crystals formed and resulted in a relatively high initial CA current signal. However, after this initial chromate formation, the oxidation reaction did not proceed further, probably due to the lack of mobile intermediates[25]. This could explain the decrease in the measured CA current (Figure 7).

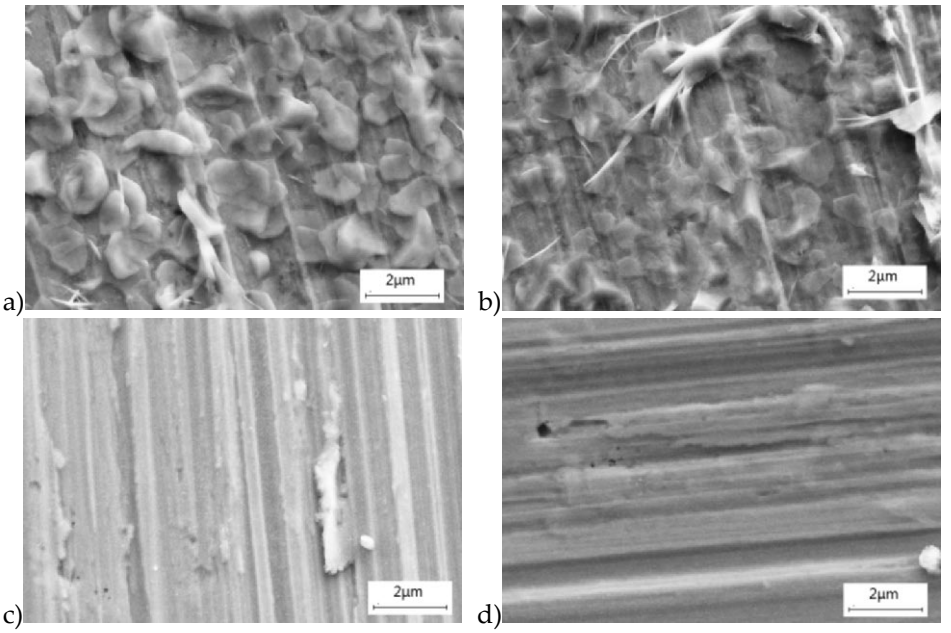

Figure 20. Secondary electron images of Sanicro 28 surfaces exposed to K_2CO_3 at 535 °C for 120 min under dry stagnant conditions. The images were taken from a) the surface under the salt pellet (location a in Fig. 5B), b) the surface on the edge of the salt pellet (location b in Fig. 5B), c) the affected surface around the salt pellet (location c in Fig. 5B), d) the unaffected surface (location d in Fig. 5B). [Paper III]

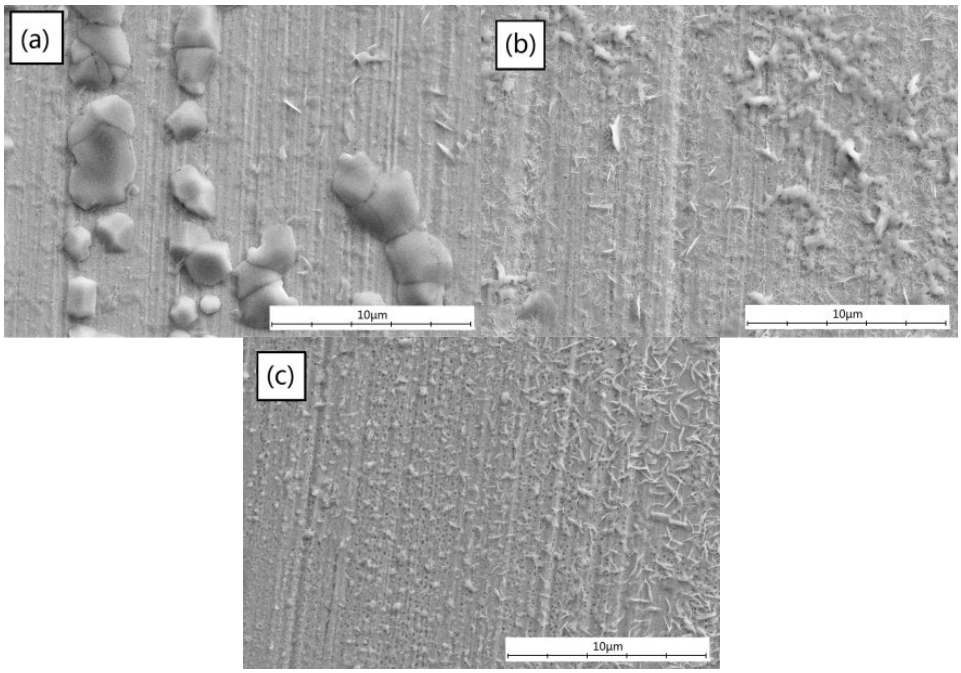

Figure 21. Secondary electron images of Sanicro 28 surfaces exposed for 120 min at 535 °C to K_2CO_3 under dry flowing conditions. The images were taken from a) the surface under the salt pellet (location a in Figure 5B), b) the surface around the salt pellet (location c in Figure 5B) and c) the surface far from the salt pellet (location d in Figure 5B). [Paper IV]

According to the CA results (Figures 6 and 7), the main difference between KCl and K_2CO_3 induced corrosion was observed at the very beginning of the reaction. In the presence of K_2CO_3, the immediate initial oxidation current was attributed to the fast potassium chromate formation. In the presence of KCl, the increasing on-going oxidation current was attributed both to potassium and chloride. The higher iron concentration of the reaction layer in the presence of KCl also supported the idea that chloride played an important role in the subsequent reactions, e.g. in the diffusion of iron from the bulk material.

4.6.2 Humid conditions

The surface morphologies of the samples exposed to K_2CO_3 under humid conditions (Figure 22) differed from the morphology observed under dry conditions (Figure 21) in terms of the crystal size and the oxide layer thickness. For the sample exposed to K_2CO_3 under humid conditions, a large amount of K_2CrO_4 crystals was identified. The surface below the

salt pellet was packed with K_2CrO_4 crystals of the same size (Figure 22a). In contrast, less but larger K_2CrO_4 crystals were observed on the steel surface around the salt pellet (Figure 22b). The surface morphology and elemental distribution indicated that the mechanisms of the corrosion reaction with K_2CO_3 were different in the dry and wet conditions. A possible reaction mechanism in the presence of water vapor is suggested: In the presence of humidity, K_2CO_3 decompose to form KOH and carbon dioxide at high temperatures (Eq. 24), as also reported in the *Corrosion Engineering and Cathodic Protection Handbook: With an Extensive Question and Answer Section*[81]. The released carbon dioxide molecules, or active carbonate ions (CO_3^{2-}) from the salt react with water vapor to produce carbonic acid (H_2CO_3) (Eq. 25)[81]. H_2CO_3 might react further with iron to iron bicarbonate ($Fe(HCO_3)_2$) (Eq. 26). Iron bicarbonate again reacts with dissolved oxygen to form iron oxide, which results in a thick and homogeneous oxide layer on the surface (Eq. 27)[81]. As the oxidation state of each element in the reactions (Eqs. 24-25 and 27) does not change, these reactions do not affect the CA oxidation current signal. In contrast, the reactions involving chromium (Eqs. 20, 21) are associated with changes in the oxidation state and thus are likely to induce changes in the CA oxidation current signal. The formation of $Fe(HCO_3)_2$ explains that in this work, a relatively low CA current signal in the initial stage was measured when water vapor was introduced into the system.

$$\mathbf{K_2CO_3\ (s) + H_2O\ (g) = 2KOH\ (s) + CO_2\ (g)} \quad \mathbf{(24)}$$

$$\mathbf{CO_2\ (g) + H_2O\ (g) = H_2CO_3\ (g)} \quad \mathbf{(25)}$$

$$\mathbf{Fe\ (s) + 2H_2CO_3\ (g) = 4\ Fe(HCO_3)_2\ (s) + H_2\ (g)} \quad \mathbf{(26)}$$

$$\mathbf{4\ Fe(HCO_3)_2\ (s) + O_2\ (g) = 2\ Fe_2O_3\ (s) + 8\ CO_2\ (g) + 4\ H_2O\ (g)} \quad \mathbf{(27)}$$

It should be noted, however, that the corrosion behavior of the two potassium salts was studied for a relatively short exposure time, two hours. A greater difference in the corrosion behavior between the alkali carbonate and the alkali chloride-induced corrosion has been reported in experiments with a longer exposure time (e.g. >24 hours)[53,54]. According to these longer experiments, chloride played an active role in the latter reaction stages after formation of alkali chromate, as expected.

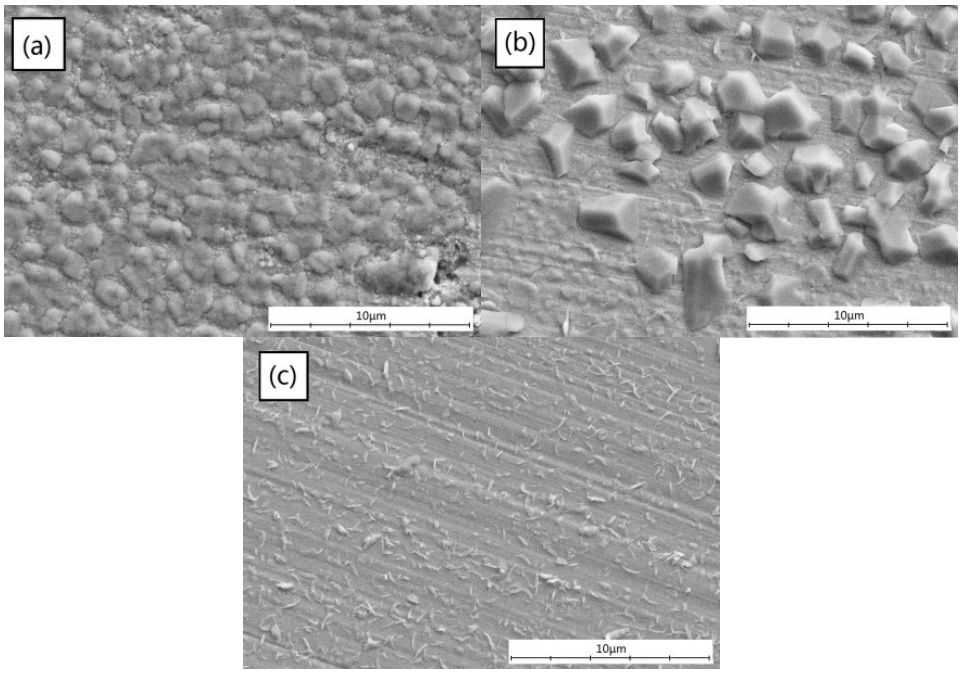

Figure 22. Secondary electron images of Sanicro 28 surfaces exposed for 120 min at 535 °C to K_2CO_3 under humid flowing conditions. The images were taken from a) the surface under the salt pellet (location a in Figure 5B), b) the surface around the salt pellet (location c in Figure 5B) and c) the surface far from the salt pellet (location d in Figure 5B). [Paper IV]

5. Conclusions

In this work, chronoamperometry (CA) was developed utilized to study the early stages of oxide layer degradation of Sanicro 28 steel in the presence of KCl, NaCl and K_2CO_3 at 450 and 535 °C under stagnant conditions and under flowing conditions. The signals from the CA were verified with SEM and XPS analyses of the samples after the exposures. The corrosion net currents measured with CA could be clearly distinguished from the background noise. The relative magnitude of these currents between samples exposed to the salts at different temperatures correlated with the reactions occurring on the surface and in the underlying material. According to the XPS and SEM measurements, the changes observed in the current signals originated from conversion and/or alteration of the passivation layer.

At both test temperatures, all three alkali salts clearly affected the steel samples. High Cr^{6+}/Cr^{3+}-ratios were detected in the area in direct contact with the salt. This indicated that all salts initiated alkali chromate formation when in contact with the sample. At 450 °C, the rates of the oxidation reactions with all studied salts were much lower than at 535 °C, which could be reflected by the much lower oxidation reaction current signal observed. Also, a thinner chromium oxide with smaller alkali chromate crystals formed on the sample surface at 450 °C. However, the Cr^{6+}/Cr^{3+} -ratio was higher at 450 °C than at 535 °C. This indicated that the initial conversion of the chromium oxide to alkali chromate was dominant at 450 °C, while at 535 °C, part of the formed alkali chromate reacted further to chromium oxide, resulting in a higher chromium oxide formation rate.

The roles of the cations (K^+ and Na^+) and anions (Cl^-, CO_3^{2-}) in the onset of the corrosion process were also explored. When comparing KCl and NaCl, similar overall elemental distributions in the oxide layer and a similar surface morphology suggested that the chloride containing salts had a similar corrosive effect on the steel. Both chlorides lead to the formation of alkali chromate, which depletes chromium in the protective oxide layer and thus makes the stainless steel more vulnerable to high temperature corrosion. However, KCl caused higher rate of the initial formation of alkali chromate compared to NaCl at 450 °C. This correlated well with the higher observed oxidation current at the steady state in the

CA measurements. Further, at 535 °C, the thickness of the formed alkali chromate crystal layer was higher in the presence of KCl than in the presence of NaCl. Further, the formed chromium and iron oxide layers were thinner in the presence of KCl than NaCl. The tested steel, Sanicro 28 exhibited higher internal degradation during exposure to NaCl than to KCl. Under the humid conditions, a greater thermodynamic driving force led to a more rapid formation of K_2CrO_4 in the presence of KCl, which due to the thermodynamically stable HCl formed during the initial stage. It was assumed that NaCl might react with iron oxide and water to form sodium ferrate (III) ($Na_2Fe_2O_4$) and hydrogen chloride. Thus, lower amount of Na_2CrO_4 and a thicker oxide layer with a higher concentration of iron formed on NaCl-exposed samples.

When comparing KCl and K_2CO_3, an oxidation reaction or a set of oxidation reactions appeared to be kinetically more favorable in the presence of K_2CO_3. Also, K_2CO_3 initiated potassium chromate formation, but the diffusion rate of K_2CO_3 was lower than that of KCl, presumably due to the lower vapor pressure of K_2CO_3. The presence of K_2CO_3 resulted in a much larger amount of K_2CrO_4 under dry stagnant and flowing conditions. The fast formation of K_2CrO_4 crystals was assumed based on the fast initial and ongoing oxidation current. However, since a suitable mobile intermediate for subsequent reactions was lacking, the rate of the oxidation current decreased. Accordingly, less amount of metal oxide formed. Under humid conditions, K_2CO_3 decomposed and formed carbon dioxide, which then reacted with water vapor to produce H_2CO_3. The formed H_2CO_3 was assumed to react with iron to iron bicarbonate ($Fe(HCO_3)_2$). The produced iron bicarbonate then reacted with the dissolved oxygen to a thick and homogeneous iron-rich oxide layer on the surface.

In addition, water with radioactively labeled oxygen (^{18}O) was used to create a humid atmosphere in the furnace and to explore whether the corrosion reactions are initiated with the oxygen in the air or oxygen in the water vapor. The ToF-SIMS analysis of the surface after the exposure to KCl and humid atmosphere suggested that the oxygen in the water had a higher reaction rate than the oxygen molecules with the chromium oxide layer. The presence of ^{18}O in the chromate crystals indicated that the humidity also played a role in the chromate formation.

The combinatory methods enable online monitoring of high temperature solid-solid reactions, providing information about the rate and the course of the reactions. Combined with the previously proposed corrosion mechanism, by studying the corrosion mechanism using the combinatory methods can provide a novel sight of identifying the species within the altered oxide layer as a function of time and temperature, thereby increasing the understanding of the onset of corrosion of heat exchanger materials. The information can give a better understanding of the onset of formation of Cr^{6+} as a function of temperature, oxide layer thickness and lateral distance from the initial area of exposure. The accessibility of the oxygen atom from molecular O_2 vs. H_2O were investigated as a function of temperature and thickness of the oxide layer.

In addition, from the industry viewpoint, this work can estimate safe operating temperatures for different steel materials in power plant environments. The suggested method is promising e.g. when estimating the interactions between deposits and heat exchanger materials and predicting the ability of these materials to resist corrosion. Thus, the results may assist in designing biomass-fired boilers with improved durability and also to optimize the operational costs.

6. Future work

Sanicro 28, a steel with a high content of chromium, was significantly corroded when in contact with alkali salts, i.e. synthetic ashes typical for biomass combustion, well below the melting points of the studied salts. As several corrosive compounds might be present in the ashes during biomass combustion, employing a high chromium material may not always be a remedy for high temperature corrosion of the boiler materials. Thus, careful consideration of fuels, the operating conditions, and the boiler designs, especially novel materials and coatings, are needed for a better corrosion resistance.

Moreover, using sulfur-containing fuel additives or co-combusting with a sulfur-rich fuel has been proven as a successful way to decrease corrosion rate of the superheater materials in the biomass boiler in the presence of the alkali salts[82–84]. The reason is that SO_x content in the flue gas can alter the corrosive deposit composition and the mechanism of ash formed, which leads to alkali salts being converted into less corrosive alkali sulfates. However, the reaction mechanism of the sulfation process of alkali salts in the biomass combustion is rather poorly understood. In future, chronoamperometry together with the surface characterization techniques could be employed for enhanced understanding of the role of SO_x in the corrosion mechanism.

7. References

1. Baede A, van der Linden P, Verbruggen A. Annex to IPCC Fourth Assessment Report. *IPCC Fourth Assess Rep*. 2007:75-104. https://www.ipcc.ch/pdf/assessment-report/ar4/syr/ar4_syr_appendix.pdf.
2. International Energy Agency I. CO2 Emissions from Fuel Combustion 2017 - Highlights. 2017. doi:10.1787/co2_fuel-2017-en.
3. Brower M, Green D, Hinrichs-rahlwes R, et al. *2014*.; 2014.
4. Tobergte DR, Curtis S. Recent Greenhouse Gas Concentrations. Journal of Chemical Information and Modeling. doi:10.1017/CBO9781107415324.004.
5. Demirbas A. Potential applications of renewable energy sources, biomass combustion problems in boiler power systems and combustion related environmental issues. *Prog Energy Combust Sci*. 2005;31(2):171-192. doi:10.1016/j.pecs.2005.02.002.
6. Ferroukhi R, Khalid A, Lopez-Peña A, Renner M. Renewable Energy and Jobs: Annual Review 2015. 2015:16. doi:http://www.irena.org/menu/index.aspx?mnu=Subcat&PriMenuID=36&CatID=141&SubcatID=585.
7. Energy supply and consumption. *Stat Finl*. 2016:1-13.
8. Vassilev S V., Baxter D, Andersen LK, Vassileva CG. An overview of the chemical composition of biomass. *Fuel*. 2010;89(5):913-933. doi:10.1016/j.fuel.2009.10.022.
9. Saidur R, Abdelaziz EA, Demirbas A, Hossain MS, Mekhilef S. A review on biomass as a fuel for boilers. *Renew Sustain Energy Rev*. 2011;15(5):2262-2289. doi:10.1016/j.rser.2011.02.015.
10. Motiva. Renewable energy in Finland. 2014:1-12. http://www.motiva.fi/files/2496/Renewable_Energy_in_Finland.pdf.
11. Khan AA, de Jong W, Jansens PJ, Spliethoff H. Biomass combustion in fluidized bed boilers: Potential problems and remedies. *Fuel Process Technol*. 2009;90(1):21-50. doi:10.1016/j.fuproc.2008.07.012.
12. Laxminarayan Y, Nair AB, Jensen PA, et al. Tensile Adhesion Strength of Biomass Ash Deposits: Effect of the Temperature Gradient and Ash Chemistry. *Energy and Fuels*. 2018;32(4):4432-4441. doi:10.1021/acs.energyfuels.7b03114.
13. Skrifvars BJ, Westén-Karlsson M, Hupa M, Salmenoja K. Corrosion of super-heater steel materials under alkali salt deposits. Part 2: SEM analyses of different steel materials. *Corros Sci*. 2010;52(3):1011-1019. doi:10.1016/j.corsci.2009.11.026.
14. Nielsen HP, Frandsen FJ, Dam-Johansen K, Baxter LL. Implications of chlorine-associated corrosion on the operation of biomass-fired boilers. *Prog Energy Combust Sci*. 2000;26(3):283-298. doi:10.1016/S0360-1285(00)00003-4.
15. Hupa M. Ash-related issues in fluidized-bed combustion of biomasses: Recent research highlights. *Energy and Fuels*. 2012;26(1):4-14. doi:10.1021/ef201169k.

16. Viklund P, Hjörnhede A, Henderson P, Stålenheim A, Pettersson R. Corrosion of superheater materials in a waste-to-energy plant. *Fuel Process Technol*. 2013;105:106-112. doi:10.1016/j.fuproc.2011.06.017.

17. Antunes RA, de Oliveira MCL. Corrosion in biomass combustion: A materials selection analysis and its interaction with corrosion mechanisms and mitigation strategies. *Corros Sci*. 2013;76:6-26. doi:10.1016/j.corsci.2013.07.013.

18. Okoro SC, Montgomery M, Frandsen FJ, Pantleon K. Effect of Water Vapor on High-Temperature Corrosion under Conditions Mimicking Biomass Firing. *Energy and Fuels*. 2015;29(9):5802-5815. doi:10.1021/acs.energyfuels.5b01045.

19. Liu S, Liu Z, Wang Y, Tang J. A comparative study on the high temperature corrosion of TP347H stainless steel, C22 alloy and laser-cladding C22 coating in molten chloride salts. *Corros Sci*. 2014;83:396-408. doi:10.1016/j.corsci.2014.03.012.

20. Bankiewicz D, Vainikka P, Lindberg D, et al. High temperature corrosion of boiler waterwalls induced by chlorides and bromides - Part 2: Lab-scale corrosion tests and thermodynamic equilibrium modeling of ash and gaseous species. *Fuel*. 2012;94:240-250. doi:10.1016/j.fuel.2011.12.023.

21. Enestam S, Bankiewicz D, Tuiremo J, Mäkelä K, Hupa M. Are NaCl and KCl equally corrosive on superheater materials of steam boilers? *Fuel*. 2013;104:294-306. doi:10.1016/j.fuel.2012.07.020.

22. Karlsson S, Pettersson J, Johansson LG, Svensson JE. Alkali Induced High Temperature Corrosion of Stainless Steel: The Influence of NaCl, KCl and CaCl2. *Oxid Met*. 2012;78(1-2):83-102. doi:DOI 10.1007/s11085-012-9293-7.

23. Shinata Y, Nishi Y. NaCl-induced accelerated oxidation of chromium. *Oxid Met*. 1986;26(3-4):201-212. doi:10.1007/BF00659184.

24. Vignarooban K, Pugazhendhi P, Tucker C, Gervasio D, Kannan AM. Corrosion resistance of Hastelloys in molten metal-chloride heat-transfer fluids for concentrating solar power applications. *Sol Energy*. 2014;103:62-69. doi:10.1016/j.solener.2014.02.002.

25. Lehmusto J, Yrjas P, Skrifvars BJ, Hupa M. High temperature corrosion of superheater steels by KCl and K 2CO 3 under dry and wet conditions. *Fuel Process Technol*. 2012;104:253-264. doi:10.1016/j.fuproc.2012.05.020.

26. Luo WW, Liu Z De, Wang YT, Yang RJ. High temperature corrosion behaviors of the superheater materials. *Procedia Eng*. 2012;36:212-216. doi:10.1016/j.proeng.2012.03.033.

27. Olsson COA, Landolt D. Passive films on stainless steels - Chemistry, structure and growth. *Electrochim Acta*. 2003;48(9 SPEC.):1093-1104. doi:10.1016/S0013-4686(02)00841-1.

28. Graham MJ, Hussey RJ. Characterization and growth of oxide films. *Corros Sci*. 2002;44(2):319-330. doi:10.1016/S0010-938X(01)00063-4.

29. Proff C, Jonsson T, Pettersson C, Svensson JE, Johansson LG, Halvarsson M. Microstructural investigation of the KCl-induced corrosion of the austenitic alloy

Sanicro 28 (35Fe27Cr31Ni) at 600°C. *Mater High Temp*. 2009;26(2):113-125. doi:10.3184/096034009X464339.

30. Skrifvars B-J, Backman R, Hupa M, Salmenoja K, Vakkilainen E. Corrosion of superheater steel materials under alkali salt deposits Part 1: The effect of salt deposit composition and temperature. *Corros Sci*. 2008;50(5):1274-1282. doi:10.1016/j.corsci.2008.01.010.

31. Pettersson J, Asteman H, Svensson JE, Johansson LG. KCl induced corrosion of a 304-type austenitic stainless steel at 600°C; the role of potassium. *Oxid Met*. 2005;64(1-2):23-41. doi:10.1007/s11085-005-5704-3.

32. Pettersson C, Jonsson T, Proff C, Halvarsson M, Svensson JE, Johansson LG. High temperature oxidation of the austenitic (35Fe27Cr31Ni) alloy sanicro 28 in O 2 + H 2O environment. *Oxid Met*. 2010;74(1-2):93-111. doi:10.1007/s11085-010-9199-1.

33. Allen GC, Harris SJ, Jutson JA, Dyke JM. A study of a number of mixed transition metal oxide spinels using X-ray photoelectron spectroscopy. *Appl Surf Sci*. 1989;37(1):111-134. doi:10.1016/0169-4332(89)90977-X.

34. Allen GC, Jutson JA, Tempest PA. Geoffrey C. ALLEN, Josephine A. JUTSON and Paul A. TEMPEST. 1988.

35. Lee YY, McNallan MJ. Ignition of nickel in environments containing oxygen and chlorine. *Metall Trans A*. 1991;18(6):1099-1107. doi:10.1007/BF03325720.

36. Grabke HJ, Reese E, Spiegel M. The effects of chlorides, hydrogen chloride, and sulfur dioxide in the oxidation of steels below deposits. *Corros Sci*. 1995;37(7):1023-1043. doi:10.1016/0010-938X(95)00011-8.

37. Spiegel M. Salt melt induced corrosion of metallic materials in waste incineration plants. *Mater Corros*. 1999;50(7):373–393. http://onlinelibrary.wiley.com/doi/10.1002/(SICI)1521-4176(199907)50:7%3C373::AID-MACO373%3E3.0.CO;2-T/abstract.

38. Mortazavi N, Intiso L, Israelsson N, Johansson L-G, Halvarsson M. In Situ ESEM Investigation of KCl-Induced Corrosion of a FeCrAl and a Model FeNiCrAl Alloy in Lab Air at 450°C. *J Electrochem Soc*. 2015;162(14):C744-C753. doi:10.1149/2.0581514jes.

39. Pan TJ, Li YS, Yang Q, Feng RF, Hirose A. Internal oxidation and phase transformations of multi-phase Fe-Ni-Al and Fe-Ni-Al-Cr alloys induced by KCl corrosion. *Corros Sci*. 2011;53(6):2115-2121. doi:10.1016/j.corsci.2011.02.034.

40. Ma HT, Zhou CH, Wang L. High temperature corrosion of pure Fe, Cr and Fe-Cr binary alloys in O2 containing trace KCl vapour at 750 °C. *Corros Sci*. 2009;51(8):1861-1867. doi:10.1016/j.corsci.2009.05.014.

41. Wu H, Yrjas P, Hupa M. Laboratory Studies of Potassium-Halide-Induced High-Temperature Corrosion of Superheater Steels. Part 1: Exposures in Dry Air. *Energy & Fuels*. 2015:150127105718003. doi:10.1021/ef502245f.

42. Dudziak T, Jura K, Rutkowska J. Chlorine Corrosion Degradation of Low Alloyed Ferritic Steels in Temperature Range 450-550°C. *Oxid Met*. 2016;85(5-6):647-664. doi:10.1007/s11085-016-9617-0.

43. Kiamehr S, Dahl K V., Montgomery M, Somers MAJ. KCl-induced high temperature corrosion of selected commercial alloys: Part II: Alumina and silica-formers. *Mater Corros*. 2016;67(1):26-38. doi:10.1002/maco.201408215.

44. Cha SC, Spiegel M. Local reactions of KCl particles with iron, nickel and chromium surfaces. *Mater Corros*. 2006;57(2):159-164. doi:10.1002/maco.200503903.

45. Jonsson T, Folkeson N, Svensson JE, Johansson LG, Halvarsson M. An ESEM in situ investigation of initial stages of the KCl induced high temperature corrosion of a Fe-2.25Cr-1Mo steel at 400°C. *Corros Sci*. 2011;53(6):2233-2246. doi:10.1016/j.corsci.2011.03.007.

46. Pettersson C, Johansson LG, Svensson JE. The influence of small amounts of KCl(s) on the initial stages of the corrosion of alloy sanicro 28 at 600 °C. *Oxid Met*. 2008;70(5-6):241-256. doi:10.1007/s11085-008-9118-x.

47. Lehmusto J, Skrifvars B-J, Yrjas P, Hupa M. High temperature oxidation of metallic chromium exposed to eight different metal chlorides. *Corros Sci*. 2011;53(10):3315-3323. doi:10.1016/j.corsci.2011.06.007.

48. Folkeson N, Jonsson T, Halvarsson M, Johansson LG, Svensson JE. The influence of small amounts of KCl(s) on the high temperature corrosion of a Fe-2.25Cr-1Mo steel at 400 and 500°C. *Mater Corros*. 2011;62(7):606-615. doi:10.1002/maco.201005942.

49. Israelsson N, Unocic KA, Hellström K, et al. A Microstructural and Kinetic Investigation of the KCl-Induced Corrosion of an FeCrAl Alloy at 600°C. *Oxid Met*. 2015;84(1-2):105-127. doi:10.1007/s11085-015-9546-3.

50. Israelsson N, Engkvist J, Hellström K, Halvarsson M, Svensson JE, Johansson LG. KCl-Induced Corrosion of an FeCrAl Alloy at 600 °C in O2 + H2O Environment: The Effect of Pre-oxidation. *Oxid Met*. 2014;83(1-2):29-53. doi:10.1007/s11085-014-9507-2.

51. Israelsson N, Unocic KA, Hellström K, Svensson JE, Johansson LG. Cyclic Corrosion and Chlorination of an FeCrAl Alloy in the Presence of KCl. *Oxid Met*. 2015;84(3-4):269-290. doi:10.1007/s11085-015-9554-3.

52. Liu J, Dyson D, Asselin E. Long-term Hot Corrosion Behavior of Boiler Tube Alloys in Waste-to-Energy Plants. *Oxid Met*. 2016;86(1-2):135-149. doi:10.1007/s11085-016-9627-y.

53. Lehmusto J, Skrifvars BJ, Yrjas P, Hupa M. Comparison of potassium chloride and potassium carbonate with respect to their tendency to cause high temperature corrosion of stainless 304L steel. *Fuel Process Technol*. 2013;105:98-105. doi:10.1016/j.fuproc.2011.12.016.

54. Pettersson J, Folkeson N, Johansson LG, Svensson JE. The effects of KCl, K 2SO 4 and K 2CO 3 on the high temperature corrosion of a 304-type austenitic stainless steel. *Oxid Met*. 2011;76(1-2):93-109. doi:10.1007/s11085-011-9240-z.

55. Jonsson T, Karlsson S, Hooshyar H, et al. Oxidation After Breakdown of the Chromium-Rich Scale on Stainless Steels at High Temperature: Internal Oxidation. *Oxid Met*. 2016;85(5):1-28. doi:10.1007/s11085-016-9610-7.

56. Lehmusto J, Lindberg D, Yrjas P, Skrifvars BJ, Hupa M. Thermogravimetric studies of high temperature reactions between potassium salts and chromium. *Corros Sci*. 2012;59:55-62. doi:10.1016/j.corsci.2012.02.013.

57. Graham MJ. The application of surface techniques in understanding corrosion phenomena and mechanisms. *Corros Sci*. 1995;37(9):1377-1397. doi:10.1016/0010-938X(95)00040-Q.

58. Retschitzegger S, Gruber T, Brunner T, Obernberger I. Short term online corrosion measurements in biomass fired boilers. Part 1: Application of a newly developed mass loss probe. *Fuel Process Technol*. 2015;137:148-156. doi:10.1016/j.fuproc.2015.03.026.

59. Retschitzegger S, Gruber T, Brunner T, Obernberger I. Short term online corrosion measurements in biomass fired boilers. Part 2: Investigation of the corrosion behavior of three selected superheater steels for two biomass fuels. *Fuel Process Technol*. 2016;142:59-70. doi:10.1016/j.fuproc.2015.09.021.

60. Mortazavi N, Intiso L, Israelsson N, Johansson LG, Halvarsson M. In situ investigation of the initial stages of KCl-induced corrosion of a chromia-forming steel at 450°C using an environmental scanning electron microscope. *Corrosion*. 2016;72(1):23-32. doi:10.5006/1874.

61. Mischler S, Vogel A, Mathieu HJ, Landolt D. Chemical composition of the passive film on Fe-24Cr and Fe-24Cr-11Mo studied by AES, XPS and SIMS. *Corros Sci*. 1991;32(9):925-944. doi:10.1016/0010-938X(91)90013-F.

62. Sasikumar Y, Rajendran N. Effect of Fluoride Concentration and pH on Corrosion Behavior of Ti–15Mo in Artificial Saliva. *J Bio- Tribo-Corrosion*. 2018;4(1):3. doi:10.1007/s40735-017-0119-7.

63. Rard JA, Platford RF. *ActiVity Coefficients in Electrolyte Solutions, ; Pitzer, KS, Ed.*; 1991.

64. Khodari M. Stripping voltammetric and conductance measurements on corrosion and inhibition of copper in nitric acid. *Mater Chem Phys*. 2001;71(3):279-290. doi:10.1016/S0254-0584(01)00291-7.

65. Foley RT, Nguyen TH. The chemical nature of aluminum corrosion. *J Electrochem Soc Electrochem Sci Technol*. 1982;129(3):464-467. doi:10.1149/1.2123768.

66. Taxil P, Mahenc J. Formation of corrosion-resistant layers by electrodeposition of refractory metals or by alloy electrowinning in molten fluorides. *J Appl Electrochem*. 1987;17(2):261-269. doi:10.1007/BF01023292.

67. Fayyad EM, Almaadeed MA, Jones A, Abdullah AM. Evaluation Techniques for the Corrosion Resistance of Self- Healing Coatings. *Int J Electrochem Sci*. 2014;9:4989-5011. www.electrochemsci.org.

68. Wildgoose GG, Giovanelli D, Lawrence NS, Compton RG. High-temperature electrochemistry: A review. *Electroanalysis*. 2004;16(6):421-433. doi:10.1002/elan.200302875.

69. Huang J, Wu X, Han EH. Electrochemical properties and growth mechanism of passive films on Alloy 690 in high-temperature alkaline environments. *Corros Sci*. 2010;52(10):3444-3452. doi:10.1016/j.corsci.2010.06.016.

70. Jüttner K. Electrochemical impedance spectroscopy (EIS) of corrosion processes on inhomogeneous surfaces. *Electrochim Acta*. 1990;35(10):1501-1508. doi:10.1016/0013-4686(90)80004-8.

71. Tan YJ, Bailey S, Kinsella B. An investigation of the formation and destruction of corrosion inhibitor films using electrochemical impedance spectroscopy (EIS). *Corros Sci*. 1996;38(9):1545-1561. doi:10.1016/0010-938X(96)00047-9.

72. Osório WR, Peixoto LC, Cant?? M V., Garcia A. Electrochemical corrosion characterization of Al-Ni alloys in a dilute sodium chloride solution. *Electrochim Acta*. 2010;55(13):4078-4085. doi:10.1016/j.electacta.2010.02.029.

73. Castillo Morquecho CP, López Meléndez C, Esparza Ponce HE, et al. Evaluation and characterization of thin films on AISI 9840 by electrochemical noise. *Int J Electrochem Sci*. 2015;10(2):1094-1101.

74. Zeng CL, Wang W, Wu WT. Electrochemical impedance models for molten salt corrosion. *Corros Sci*. 2001;43(4):787-801. doi:10.1016/S0010-938X(00)00108-6.

75. Liu L, Li Y, Wang F. Pitting mechanism on an austenite stainless steel nanocrystalline coating investigated by electrochemical noise and in-situ AFM analysis. *Electrochim Acta*. 2008;54(2):768-780. doi:10.1016/j.electacta.2008.06.076.

76. Hong T, Jepson WP. Corrosion inhibitor studies in large flow loop at high temperature and high pressure. *Corros Sci*. 2001;43(10):1839-1849. doi:10.1016/S0010-938X(01)00002-6.

77. Rihan RO, Nešić S. Erosion-corrosion of mild steel in hot caustic. Part II: The effect of acid cleaning. *Corros Sci*. 2006;48(9):2660-2675. doi:10.1016/j.corsci.2005.09.019.

78. Hermas AA. XPS analysis of the passive film formed on austenitic stainless steel coated with conductive polymer. *Corros Sci*. 2008;50(9):2498-2505. doi:10.1016/j.corsci.2008.06.019.

79. Baer, Donald R. et al. Baer, Donald R., et al. "Comparison of the sputter rates of oxide films relative to the sputter rate of SiO2." *J Vac Sci Technol A*. 28(5):1060-1072.

80. Lu Q, Hultquist G. A comparison of the initial reaction of pure Fe, Cr and Al in H216O/H218O/O2 gas mixtures at 300–730 K studied in situ with sims. *Corros Sci*. 1994;36(6):927-939. doi:10.1016/0010-938X(94)90195-3.

81. Cicek V. *Corrosion Engineering and Cathodic Protection Handbook: With an Extensive Question and Answer Section*. John Wiley & Sons; 2017.

82. Karlsson S, Jonsson T, Josefin H, Svensson J-E, Liske J. Mitigation of Fireside Corrosion of Stainless Steel in Power Plants : A Laboratory Study of the In fl uences of SO 2 and KCl on Initial Stages of Corrosion. *Energy & Fuels*. 2014;28(5):3102-3109. doi:10.1021/ef402127h.

83. Karlsson S, Larsson E, Jonsson T, Svensson J-E, Liske J. A Laboratory Study of the in Situ Sulfation of Alkali Chloride Rich Deposits: Corrosion Perspective. *Energy & Fuels*. 2016:acs.energyfuels.6b00372. doi:10.1021/acs.energyfuels.6b00372.

84. Karlsson S, Åmand LE, Liske J. Reducing high-temperature corrosion on high-alloyed stainless steel superheaters by co-combustion of municipal sewage sludge in a fluidised bed boiler. *Fuel*. 2015;139:482-493. doi:10.1016/j.fuel.2014.09.007.

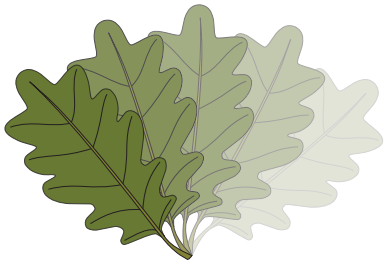

Johan Gadolin
Process Chemistry Centre

ISBN 978-952-12-3869-7